THE PENNSYLVANIA STATE UNIVERSITY
SCHREYER HONORS COLLEGE

DEPARTMENT OF ENGINEERING SCIENCE AND MECHANICS

NON-EXHIBITION OF BRAGG PHENOMENON BY CHEVRONIC SCULPTURED THIN FILMS: EXPERIMENT AND THEORY

VIKAS VEPACHEDU
SPRING 2018

A thesis
submitted in partial fulfillment
of the requirements
for a honors baccalaureate
degree in Engineering Science

Reviewed and approved* by the following:

Dr. Akhlesh Lakhtakia
The Charles Godfrey Binder (Endowed) Professor of Engineering Science and Mechanics
Professor, Graduate Program in Materials
Thesis Supervisor

Dr. Lucas J. Passmore
Assistant Teaching Professor of Engineering Science and Mechanics
Honors Adviser

Judith A. Todd
Department Head
P. B. Breneman Chair
Professor of Engineering Science and Mechanics

*Signatures are on file in the Schreyer Honors College.

Abstract

The unit cell of a chevronic sculptured thin film (ChevSTF) comprises two identical columnar thin films (CTFs) except that the nanocolumns of the first are oriented at an angle χ and nanocolumns of the second are oriented at an angle $\pi - \chi$ with respect to the interface of the two CTFs. A ChevSTF containing 10 unit cells was fabricated using resistive-heating physical vapor deposition of zinc selenide. Planewave reflectance and transmittance spectrums of this ChevSTF were measured for a wide variety of incidence conditions over the 500–900-nm range of the free-space wavelength. Despite its structural periodicity, the ChevSTF did not exhibit the Bragg phenomenon. Theoretical calculations with the CTFs modeled as biaxial dielectric materials indicated that the Bragg phenomenon would not be manifested for normal and near-normal incidence, but vestigial manifestation was possible for sufficiently oblique incidence. Thus, structural periodicity does not always lead to electromagnetic periodicity that underlies the exhibition of the Bragg phenomenon.

Table of Contents

List of Figures

Acknowledgements

Firstly, I would like to thank my thesis supervisor, Dr. Akhlesh Lakhtkia. After taking me on as his only undergraduate researcher, he invested many hours in my education to give me a genuine taste of what it means to do research. In doing so, he has helped me become a published researcher with a strong practical and theoretical background in nanoengineering. He was also never afraid to show me the truth of how difficult research is and this is perhaps what I appreciate the most for two simple reasons: it developed in me a hard-working, persistent spirit and it helped clarify my professional goals after graduation. As tiring as it was to do research, Dr. Lakhtakia was always there to encourage me and keep me on track.

Secondly, I would like to thank my lab mate Patrick McAtee for his patience as he taught me how to use the fabrication system in the lab to deposit the various thin films I was required to fabricate. When I first joined the lab, despite the rigor of his own workload, he spent many hours instructing me to ensure that I completed my tasks in a safe manner.

Chapter 1

Introduction

The following thesis is based partly on a journal publication which I authored which goes by the same title [1]. The publication was authored by me, Patrick D. McAtee and Dr. Akhlesh Lakhtakia. I was responsible for fabricating and optically characterizing the thin film samples used in the study. Dr. Lakhtakia supervised all aspects of this research and wrote the final form of the paper. Patrick D. McAtee captured the SEM images and worked with me to write the content in chapter 2. The three of us worked together to complete the other chapters. In this introductory chapter, I wrote additional sections titled “Bragg Mirrors” and “Physical Vapor Deposition” to create a more comprehensive review of the subject matter of this thesis.

1.1 The Bragg Phenomenon

The reflection of X rays of a specific wavelength incident on a crystal from a specific direction is intensely peaked in specific directions that are characteristic of the structural periodicity of the arrangement of atoms in the crystal. A simple relationship describing this phenomenon is attributed to the father-son duo W. H. Bragg and W. L. Bragg [2, 3]. The underlying mathematical treatment deriving from a rigorous application of the frequency-domain Maxwell equations was provided by Ewald [4].

The Bragg phenomenon is exhibited also by a periodically nonhomogeneous material, albeit at optical and lower frequencies [5, 6, 7]. Plane waves incident from any direction in a certain sector of the full solid angle are highly reflected by a half space occupied by a periodically nonhomogeneous material, provided that the free-space wavelength lies in a certain spectral regime, thereby indicating the formation of partial bandgaps. If high reflectance occurs for all directions in a certain spectral regime, a full bandgap is said to be exhibited.

1.2 Bragg Mirrors

Periodically nonhomogeneous materials have been commonly called as photonic crystals for the last three decades. The optical response characteristics of one-dimensional photonic crystals in the form of periodic multilayers were investigated in the late 19th century [8]. Often called Bragg mirrors or distributed Bragg reflectors nowadays, these structures are fabricated by a variety of thin-film techniques [9, 12, 10, 11]. The number N of periods must be sufficiently high for the Bragg phenomenon to be exhibited well enough for most applications [25].

When a Bragg mirror comprises only isotropic dielectric materials, its performance is independent of the polarization state of normally incident light. For obliquely incident light, the center wavelengths of the high-reflectance bands—called Bragg regimes—do not depend on the polarization state of the incident light, but the reflectance does [25].

When a Bragg mirror comprises anisotropic dielectric materials, then the exhibition of the Bragg phenomenon can be polarization dependent even for normally incident light [9, 22]. The simplest anisotropic dielectric material is uniaxial [23], as exemplified by minerals such as calcite, tourmaline, and rutile [24]. Columnar thin films (CTFs) fabricated using a variety of physical vapor deposition (PVD) techniques [10, 9, 25] are also anisotropic dielectric materials that are used in polarization-discriminatory Bragg mirrors [9, 12].

In the following section, I will discuss the problem of constructive interference caused by a thin, isotropic film on a reflective substrate as it provides some intuition for the basis of the Bragg phenomenon in Bragg mirrors.

1.2.1 Simple Thin Film Interference

Consider a beam of light incident on the sample as shown in Fig. 1.1 below. Note that all three materials shown in this figure are assumed to be isotropic. First, light which passes through the ambient environment (the layer with a refractive index of n_1) will be partially reflected by the interface with the thin film and partially transmitted into the film. Once again, at the interface between the thin film and the substrate, some more light will be reflected away. The key to creating constructive interference is to design the thicknesses of the layers such that the portion of the light which is reflected back out by the substrate (Beam B) is in-phase with the portion which is reflected back by the thin film (Beam A).

An additional consideration is the following. When light is reflected off of a medium with a higher refractive index than the originating medium, then the phase of the light changes by 180 deg. Therefore, in the case shown in Fig. 1.1, there would be such phase shifts for the beams reflecting off of the substrate and the thin film. As it turns out, since we are trying to find the phase difference between beams A and B, these two phase shifts will cancel out and are not important here.

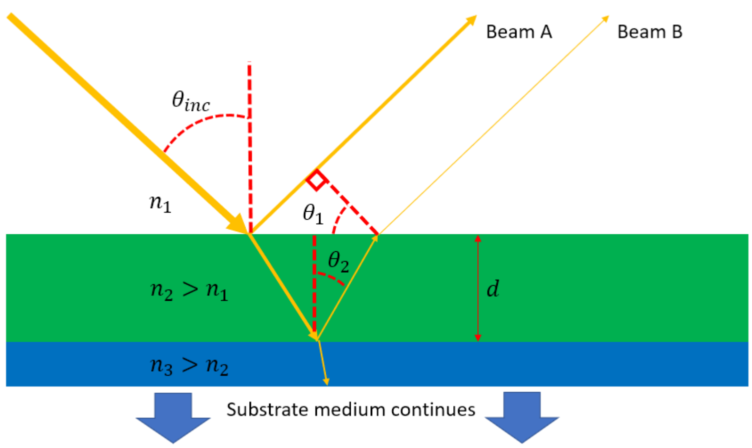

Figure 1.1: A schematic of the reflection of light in a simple thin film. The white medium is mean to be the ambient environment (such as air). The green layer is the thin film. The blue layer is the substrate. All three materials are assumed to be isotropic.

The phases of two waves can be conveniently compared using a quantity known as the optical path length: $L_{op} = nd$ where n is the refractive index of the material and d is the distance a wave travels through the said material [13]. Recall that the refractive index can be written as the ratio of the wavelength of a wave in free space to that of the wave propagating through the material in question: $n = \frac{\lambda_o}{\lambda_n}$ where λ_o is the free space wavelength and λ_n is the wavelength for the medium in question. Substituting this into the definition for the optical path length:

$$L_{op} = \lambda_o \frac{d}{\lambda_n}. \tag{1.1}$$

In Eq. 1.1 above, the quantity represented by the fraction is basically the number of wavelengths which fit in the distance traversed by the wave of light. When we multiply this quantity by the free space wavelength, we are, in a sense, scaling the number of wavelengths traversed by the free space wavelength which serves as a good reference point with which to compare phases of different light waves with. Mathematically, we can state the condition for constructive interference in this thin film in terms of the difference between optical path lengths for beams A and B shown in Fig. 1.1 [13]:

$$\Delta L_{op} = \frac{2\,d\,n_2}{cos(\theta_2)} - 2\,d\,n_1\,tan(\theta_2)\,sin(\theta_1). \tag{1.2}$$

Eq. 1.2 shows the optical path difference (OPD). This must be equal to an integer multiple of the wavelength of the light, as seen by the medium with refractive index n_1, in order for constructive interference to occur. Shown below is the final equation which describes the condition for the constructive interference of light of a certain wavelength. These are the wavelengths which would be reflected away by the sample which now acts as a basic Bragg mirror [13]:

$$2\,n_2\,d\,cos(\theta_2) = m\,\lambda. \tag{1.3}$$

In concept, expanding the structure shown in Fig. 1.1 is fairly simple. Firstly, the substrate would no longer be a substrate but a specially designed thin film layer which, in conjunction with the layer above it, would form a unit cell. The thicknesses of the two layers in the unit cell would be adjusted such that light which reflects off of the bottom of the unit cell would constructively interfere with “Beam A”. By stacking many such unit cells on top of each other, one can “catch” more light to use for constructive interference [14]. Deriving the actual transmission and reflection of light through a Bragg mirror requires more sophisticated calculations, especially if the layers in the unit cell are not isotropic. Such calculations will be used in detail in sections 2.1 and 2.2.

A noteworthy observation from Eq. 1.3 is the effect of the angle of incidence on the center wavelength of the Bragg phenomenon. Referring back to Fig. 1.1, when θ_{inc} is reduced, so is θ_2. In Eq. 1.3, when θ_2 is reduced, λ must be larger to maintain the equality. Therefore, the smaller the angle of incidence, the larger the wavelength at which the Bragg phenomenon occurs. This trend is also apparent in Bragg mirrors as it will be for the experimental and theoretical data in this study [15].

1.2.2 Design of Bragg Mirrors

For this subsection, I will discuss the design parameters of Bragg mirrors which are composed of alternating, isotropic layers (as shown in Fig. 1.2) and how these parameters affect the performance of the device. For this type of architecture, there are three main design parameters: the number of unit cells, the difference in refractive indexes of the two materials, and the respective thicknesses of each of the two layers in the unit cell. These relationships can be applied to Bragg mirrors composed of anisotropic materials as well, to a large extent.

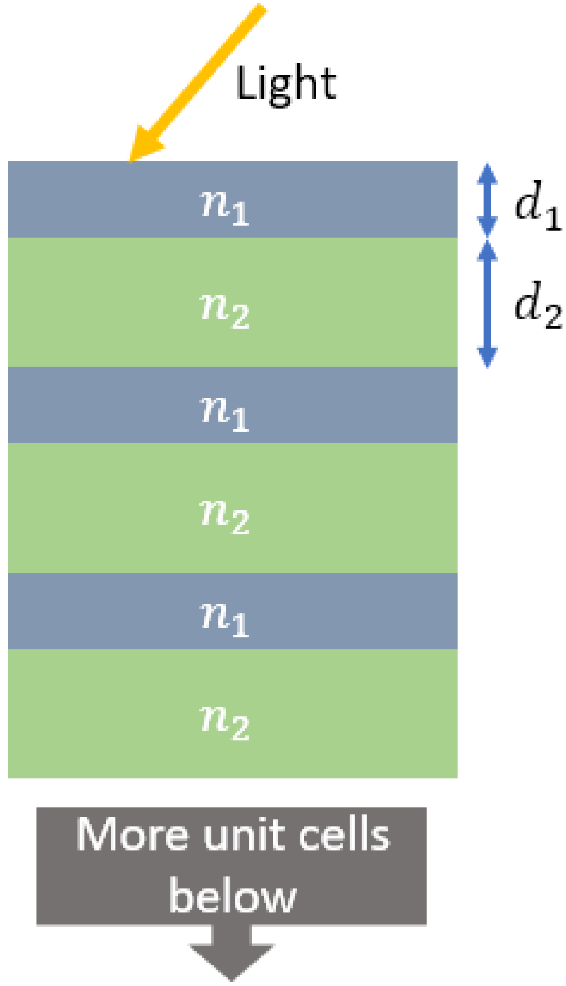

Figure 1.2: A diagram of a simple Bragg mirror in which each unit cell is a pair of isotropic materials with differing refractive indexes and thicknesses.

Firstly, the number of unit cells in a Bragg mirror affects how well developed the Bragg regime is. For light incident on one or a few unit cells, one may observe a broadened peak in the reflection of light around the center wavelength. For a well-developed Bragg mirror with a thickness on the order of 20 unit cells, the Bragg regime is very sharply defined; the reflectance sharply rises at the beginning of the optical bandgap, remains mostly flat, and quickly drops down to the original reflectance pattern [15]. This effect of the number of unit cells has been illustrated using theoretical simulations in Fig. 1.3. This figure shows the graphs of theoretical reflectances for three different Bragg mirrors. All three mirrors are identical except in the number of unit cells they are composed of. From top to bottom, the results are shown for devices made from 10, 20, and 30 unit cells. Note how increasing the number of unit cells not only raises the reflectance but also sharpens the bandgap profile.

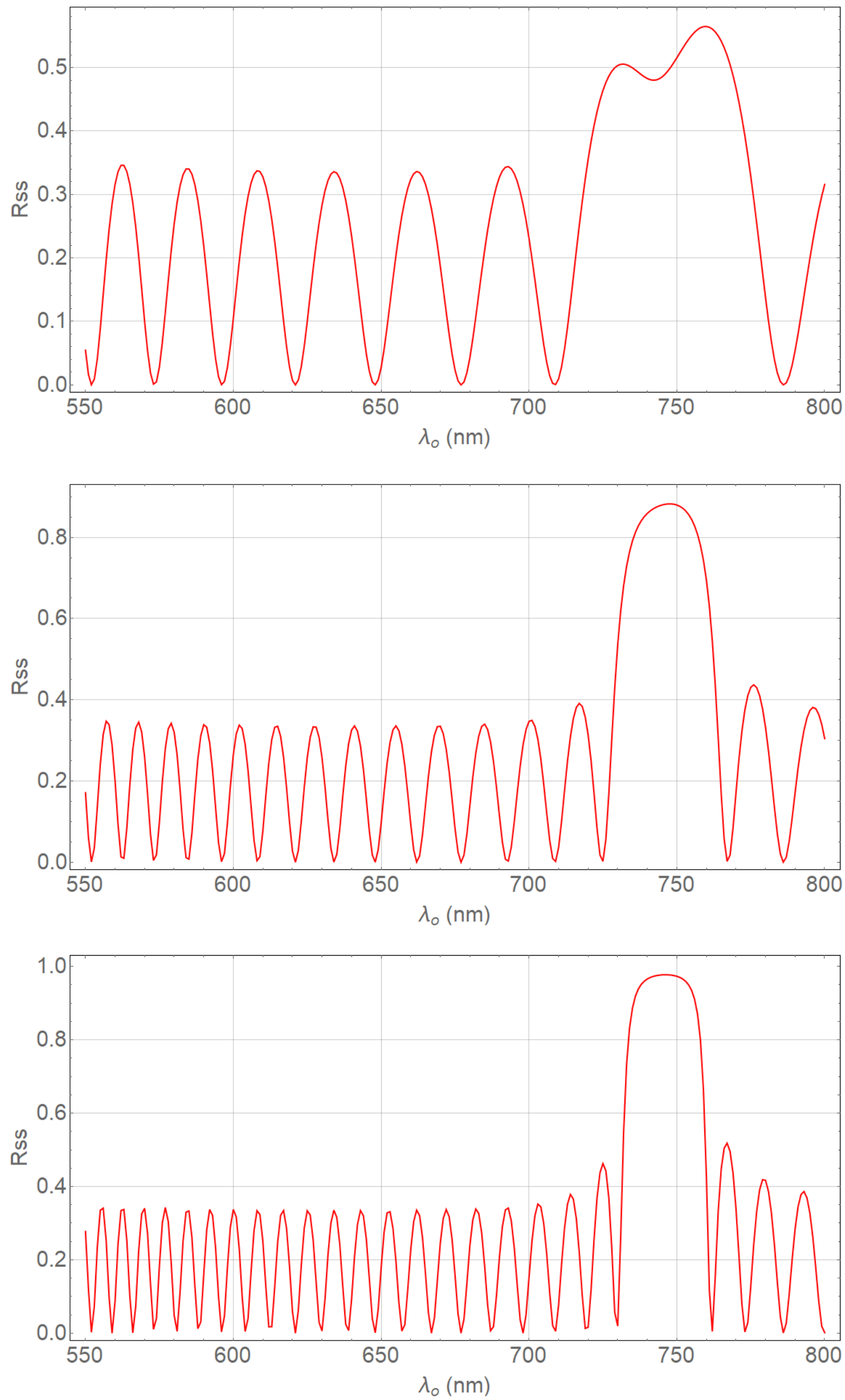

Figure 1.3: These plots show the theoretical results for the reflection of s-polarized light at different wavelengths from three Bragg mirrors. The mirrors are identical in every way except in the number of unit cells they are composed of. From top to bottom, the results are shown for a 10-, 20-, and 30-period film.

Secondly, increasing the difference in refractive indexes between the two layers in the unit cell (Δn) would make the device more effective at reflecting light. In other words, to achieve a certain level of reflectivity, one can use many unit cells with a small Δn or fewer unit cells with a large Δn. Furthermore, the width of the bandgap increases with Δn [15].

Last, but certainly not least, the choice of materials is critical. This is not only for setting a certain Δn as mentioned above, but also to account for the differing properties of these materials in different wavelength ranges (such as transmission of light). For instance, SiO_2 and Al_2O_3 are used in the visible and near-infrared regime while materials like ZnSe and Ge are used in the mid- to far-infrared [16]. This is choice is partly due to the transmission of light; SiO_2, for example, strongly absorbs light in the mid- to far-infrared range while ZnSe does not. Another factor to consider how the refractive index changes at different wavelengths; it could be that the refractive index changes drastically beyond a certain wavelength. If so, this may cause drastic changes in how the reflector operates. Shown in Fig. 1.4 are graphs of the refractive index of Ge over different wavelength ranges. Note the drastic change in refrative index between 500 and 600 nm (left) and contrast this with its relatively stable refractive index in the infrared range (right). This shows that Ge can behave fairly predictably as an optical material in the mid- to far-infrared range because its refractive index can be taken as a constant.

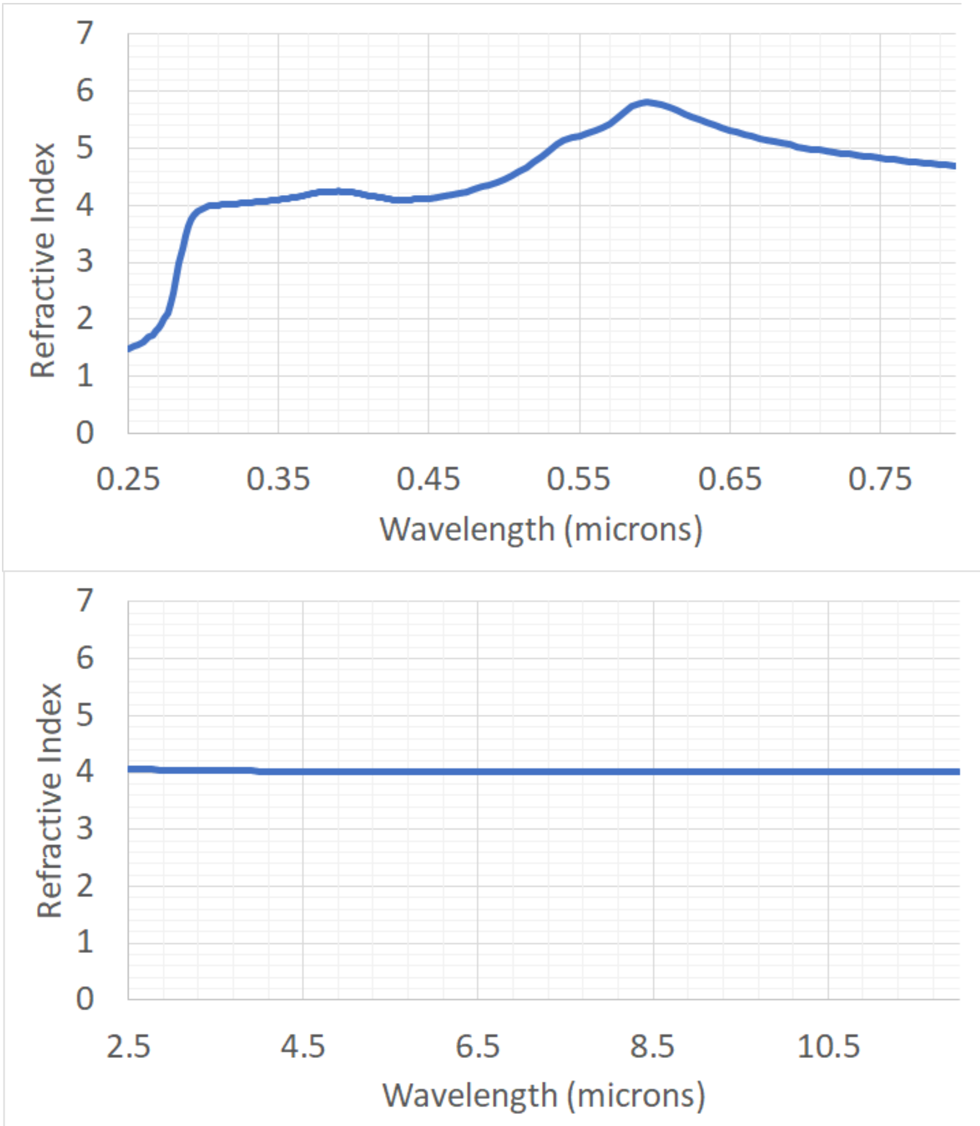

Figure 1.4: The data on the left shows the refractive index of Ge over some portion of the UV and all of the visible range. This data was obtained from: *D.E. Aspnes and A. A. Studna. Dielectric functions and optical parameters of Si, Ge, GaP, GaAs, GaSb, InP, InAs, and InSb from 1.5 to 6.0 eV, Phys. Rev. B 27, 985-1009 (1983)*. On the right is the same data but for the infrared range and it was obtained from: *Icenogle et al. Refractive indexes and temperature coefficients of germanium and silicon Appl. Opt. 15 2348-2351 (1976).*

1.2.3 Applications

Bragg reflection is used often in optical fibers to process signals of certain wavelengths. This is done by creating fiber Bragg gratings (FBGs) within the fiber. Similar in architecture to the device shown in Fig. 1.2, FBGs are portions of a fiber which are designed to have layers with alternating refractive indexes so as to reflect a certain wavelength of light. Unlike with a Bragg mirror, these gratings are not made by depositing thin films of high and low refractive index materials. Rather, one can induce permanent changes in specific portions of the glass itself by exposing these areas to certain wavelengths of light (typically ultraviolet wavelengths). In practice, two beams of light which are of this wavelength are combined to create an interference pattern on the fiber, which creates a period variation of the intensity of the light over its length. This periodic variation of the intensity subsequently induces periodic changes in the refractive index of the fiber. However, the difference between the highest and lowest refractive index is not quite as high as what one could achieve using thin films [15]. Recall from section 1.2.2 that in order to achieve a strong reflectance profile, one must at least have a large Δn with a few unit cells or a small Δn with many unit cells. In the case of FBGs, the Δn is typically small so the total length of the grating must be relatively larger (on the order of millimeters) [17, 18].

Bragg reflectors in thin-film form are used ubiquitously because of the versatility and accuracy with which one can process light with them. For instance, they can be used in extreme ultraviolet (EUV) lithography for reflecting the EUV radiation [19]. EUV lithography is a rising, next-generation form of optical lithography which is meant to enable higher resolution than current optical lithography techniques. It is highly sought after in the nanoelectronics industry because of its potential use in fabricating smaller devices. An important aspect of this technology is that lenses would actually absorb EUV radiation and, therefore, one can only use mirrors. However, the only way to create a mirror for reflecting EUV light is through a Bragg mirror composed of Si and Mo [20]. For this reason, Bragg mirrors become essential in this line of work.

Thin-film Bragg reflectors can be used once again in optical communications as a way of demultiplexing signals. In other words, multiple reflectors can be used to create a device where optical signals of different wavelengths can be separated. These reflectors are also used in fluorescence microscopy to filter out unwanted fluorescent signals [17]. Other areas where Bragg reflectors are used include but are not limited to astronomy, laser physics, and for heat control (by reflecting infrared radiaition) [21].

1.3 Physical Vapor Deposition

Physical vapor deposition (PVD) is one of the most basic techniques for fabricating thin film coatings which has been explored since the 1850s [16]. One of the ways to perform this type of deposition is by thermally evaporating the thin film material to have it deposited on the surface of a substrate. Since this is the method used in our study, the following explanation will focus on the basics of our implementation of thermal evaporation and the finer details will be explained in section 2.3.1.

The material to be deposited (ZnSe in this case) starts out in a powder form. This powdered ZnSe is packed into a tungsten receptacle from which it will be heated and evaporated. The tungsten receptacle is fixed to electrical contacts and, during the deposition process, current is passed through the receptacle. Due to tungsten's electrical resistance, much of the current's power is dissipated as heat and light (just as for the tungsten filaments in classic incandescent light bulbs). This heat is what evaporates the ZnSe and causes it to be deposited on to the substrate secured above it.

The deposition must also be performed in a high vacuum. Firstly, this ensures that the generated vapor flux travels directly to the substrate uninhibited by collisions with other gas molecules and this ensures that the deposited film is uniform. In addition, one can avoid the contamination of the film by gases such as nitrogen and oxygen.

1.4 Research Objective

As mentioned previously, the unit cell of the simplest Bragg mirror comprises two homogeneous layers of dissimilar materials. The relative permittivity dyadics [23] of the two materials must differ in their eigenvalues and/or eigenvectors. But those differences may not be sufficient for the Bragg phenomenon to be exhibited, as has been exemplified by Slepyan and Maksimenko for the following case [26]. Let a Bragg mirror occupy the region $0 < z < NP$, where $N \gg 1$, $P = 2L$ is the period of the unit cell, and L is the thickness of each of the two layers in the unit cell. Furthermore, let the relative permittivity dyadics of the materials in the two layers be denoted by

$$\left.\begin{array}{l} \underline{\underline{\varepsilon}}_1 = \underline{\underline{S}}_{\mathrm{y}}(\chi) \bullet \underline{\underline{\varepsilon}}^{o}_{ref} \bullet \underline{\underline{S}}^{T}_{\mathrm{y}}(\chi) \\ \underline{\underline{\varepsilon}}_2 = \underline{\underline{S}}_{\mathrm{y}}(\pi-\chi) \bullet \underline{\underline{\varepsilon}}^{o}_{ref} \bullet \underline{\underline{S}}^{T}_{\mathrm{y}}(\pi-\chi) \end{array}\right\}, \tag{1.4}$$

where the dyadic

$$\underline{\underline{\varepsilon}}^{o}_{ref} = \varepsilon_{\mathrm{a}}\left(\underline{\underline{I}} - \hat{\mathbf{u}}_{\mathrm{x}}\hat{\mathbf{u}}_{\mathrm{x}}\right) + \varepsilon_{\mathrm{b}}\hat{\mathbf{u}}_{\mathrm{x}}\hat{\mathbf{u}}_{\mathrm{x}} \tag{1.5}$$

contains the eigenvalues ε_{a} and ε_{b} common to both $\underline{\underline{\varepsilon}}_1$ and $\underline{\underline{\varepsilon}}_2$, $\underline{\underline{I}} = \hat{\mathbf{u}}_{\mathrm{x}}\hat{\mathbf{u}}_{\mathrm{x}} + \hat{\mathbf{u}}_{\mathrm{y}}\hat{\mathbf{u}}_{\mathrm{y}} + \hat{\mathbf{u}}_{\mathrm{z}}\hat{\mathbf{u}}_{\mathrm{z}}$ is the identity dyadic, the dyadic

$$\underline{\underline{S}}_{\mathrm{y}}(\xi) = \hat{\mathbf{u}}_{\mathrm{y}}\hat{\mathbf{u}}_{\mathrm{y}} + (\hat{\mathbf{u}}_{\mathrm{x}}\hat{\mathbf{u}}_{\mathrm{x}} + \hat{\mathbf{u}}_{\mathrm{z}}\hat{\mathbf{u}}_{\mathrm{z}})\cos\xi + (\hat{\mathbf{u}}_{\mathrm{z}}\hat{\mathbf{u}}_{\mathrm{x}} - \hat{\mathbf{u}}_{\mathrm{x}}\hat{\mathbf{u}}_{\mathrm{z}})\sin\xi \tag{1.6}$$

indicates a rotation by an angle ξ about the y axis in the xz plane, and the superscript ^{T} denotes the transpose. Equations (1.4) and (1.5) indicate that chosen Bragg mirror comprises two uniaxial dielectric materials that are identical except that the optical axis of the first material is oriented at an angle $\chi \in [0, \pi/2)$ with respect to the $+x$ axis and the optical axis of the second material is oriented at an angle $\pi - \chi$ with respect to the $+x$ axis. The optical axes of both materials lie wholly in the xz plane. Provided that the wave vector of the incident light is also wholly confined to the xz plane, theory shows that no reflection or transmission can occur at the interface of the two materials [26, 27], which implies the absence of the Bragg phenomenon [26].

The aim in this study was to verify that theoretical finding of Slepyan and Maksimenko [26]. For that purpose I fabricated a Bragg mirror made of $N = 10$ unit cells. As this fabrication was accomplished using thermal evaporation [10, 25], a PVD technique, each layer was a CTF with [9, 22]

$$\underline{\underline{\varepsilon}}^{o}_{ref} = \varepsilon_{\mathrm{b}}\hat{\mathbf{u}}_{\mathrm{x}}\hat{\mathbf{u}}_{\mathrm{x}} + \varepsilon_{\mathrm{c}}\hat{\mathbf{u}}_{\mathrm{y}}\hat{\mathbf{u}}_{\mathrm{y}} + \varepsilon_{\mathrm{a}}\hat{\mathbf{u}}_{\mathrm{z}}\hat{\mathbf{u}}_{\mathrm{z}} \tag{1.7}$$

instead of Eq. (1.5). Thus both layers in the unit cell contained a biaxial dielectric material with $\varepsilon_{\mathrm{a}} \neq \varepsilon_{\mathrm{b}} \neq \varepsilon_{\mathrm{c}}$. In each period, the nanocolumns of the first CTF are oriented at an angle χ and nanocolumns of the second CTF are oriented at an angle $\pi - \chi$ with respect to the interface of the two CTFs. As the unit cell thus has a chevronic morphology, the Bragg mirror can be classified as a chevronic sculptured thin film (ChevSTF) [25]. Furthermore, I performed optical characterization experiments with the wave vector of the incident plane wave oriented arbitrarily with respect to the xz plane. Thus, our experimental study was more general than the theoretical investigation of Slepyan and Maksimenko [26]. A theoretical exercise with Eq. (1.7) was also performed in order to qualitatively validate our experimental findings.

The plan of this paper is as follows: chapter 2 describes the experimental and theoretical techniques which were adopted to investigate the optical response characteristics of ChevSTFs, whose cell comprises two CTFs described by Eqs. (1.4) and (1.7). chapter 3 presents our experimentally obtained optical data which are compared qualitatively with the results of our theoretical exercise. Finally, chapter 4 provides concluding remarks. An $\exp(-i\omega t)$ time-dependence is implicit, with ω as the angular frequency, $i = \sqrt{-1}$, and t as time. The free-space wavenumber, the free-space wavelength, and the intrinsic impedance of free space are denoted by $k_0 = \omega\sqrt{\varepsilon_0\mu_0}$, $\lambda_0 = 2\pi/k_0$, and $\eta_0 = \sqrt{\mu_0/\varepsilon_0}$, respectively, with μ_0 and ε_0 being the permeability and permittivity of free space.

Chapter 2

Methods

2.1 Reflectances and Transmittances

The investigated problem can be theoretically formulated as follows. Suppose the region $0 < z < NP$ is occupied by a periodic multilayer of infinite transverse extent. The electric and magnetic field phasors of the plane wave incident on the periodic multilayer from the half space $z < 0$ are given by [25]

$$\left.\begin{aligned} \mathbf{E}_{\mathrm{inc}}(x,y,z) &= (a_{\mathrm{s}}\hat{\mathbf{s}} + a_{\mathrm{p}}\hat{\mathbf{p}}_{+})\,\exp\left\{ik_0\left[(x\cos\psi + y\sin\psi)\sin\theta_{\mathrm{inc}} + z\cos\theta_{\mathrm{inc}}\right]\right\} \\ \mathbf{H}_{\mathrm{inc}}(x,y,z) &= \eta_0^{-1}\,(a_{\mathrm{s}}\hat{\mathbf{p}}_{+} - a_{\mathrm{p}}\hat{\mathbf{s}})\,\exp\left\{ik_0\left[(x\cos\psi + y\sin\psi)\sin\theta_{\mathrm{inc}} + z\cos\theta_{\mathrm{inc}}\right]\right\} \end{aligned}\right\}, \quad z < 0\,, \tag{2.1}$$

where $\theta_{\mathrm{inc}} \in [0^\circ, 90^\circ)$ is the angle of incidence with respect to the z axis, $\psi \in [0^\circ, 360^\circ)$ is the angle of incidence with respect to the x axis in the xy plane, a_s is the amplitude of the s-polarized component of the plane wave, and a_p is the amplitude of the p-polarized component of the plane wave. Here and hereafter, the unit vectors

$$\left.\begin{aligned} \hat{\mathbf{s}} &= -\hat{\mathbf{u}}_{\mathrm{x}}\sin\psi + \hat{\mathbf{u}}_{\mathrm{y}}\cos\psi \\ \hat{\mathbf{p}}_{\pm} &= \mp(\hat{\mathbf{u}}_{\mathrm{x}}\cos\psi + \hat{\mathbf{u}}_{\mathrm{y}}\sin\psi)\cos\theta_{\mathrm{inc}} + \hat{\mathbf{u}}_{\mathrm{z}}\sin\theta_{\mathrm{inc}} \end{aligned}\right\} \tag{2.2}$$

delineate the orientations of the field phasors.

The electric and magnetic field phasors of the reflected plane wave are given by [25]

$$\left.\begin{aligned} \mathbf{E}_{\mathrm{ref}}(x,y,z) &= (r_{\mathrm{s}}\hat{\mathbf{s}} + r_{\mathrm{p}}\hat{\mathbf{p}}_{-})\,\exp\left\{ik_0\left[(x\cos\psi + y\sin\psi)\sin\theta_{\mathrm{inc}} - z\cos\theta_{\mathrm{inc}}\right]\right\} \\ \mathbf{H}_{\mathrm{ref}}(x,y,z) &= \eta_0^{-1}\,(r_{\mathrm{s}}\hat{\mathbf{p}}_{-} - r_{\mathrm{p}}\hat{\mathbf{s}})\,\exp\left\{ik_0\left[(x\cos\psi + y\sin\psi)\sin\theta_{\mathrm{inc}} - z\cos\theta_{\mathrm{inc}}\right]\right\} \end{aligned}\right\}, \quad z < 0\,, \tag{2.3}$$

and the electric and magnetic field phasors of the transmitted plane wave by [25]

$$\left.\begin{aligned} \mathbf{E}_{\mathrm{tr}}(x,y,z) &= (t_{\mathrm{s}}\hat{\mathbf{s}} + t_{\mathrm{p}}\hat{\mathbf{p}}_{+})\,\exp\left\{ik_0\left[(x\cos\psi + y\sin\psi)\sin\theta_{\mathrm{inc}} + (z-NP)\cos\theta_{\mathrm{inc}}\right]\right\} \\ \mathbf{H}_{\mathrm{tr}}(x,y,z) &= \eta_0^{-1}\,(t_{\mathrm{s}}\hat{\mathbf{p}}_{+} - t_{\mathrm{p}}\hat{\mathbf{s}})\,\exp\left\{ik_0\left[(x\cos\psi + y\sin\psi)\sin\theta_{\mathrm{inc}} + (z-NP)\cos\theta_{\mathrm{inc}}\right]\right\} \end{aligned}\right\}, \quad z > NP\,. \tag{2.4}$$

The reflection amplitudes r_{s} and r_{p}, as well as the transmission amplitudes t_{s} and t_{p}, have to be determined in terms of the incidence amplitudes a_{s} and a_{p} in order to find the reflection and transmission coefficients that appear as the elements of the 2×2 matrixes in the following relations:

$$\begin{bmatrix} r_{\mathrm{s}} \\ r_{\mathrm{p}} \end{bmatrix} = \begin{bmatrix} r_{\mathrm{ss}} & r_{\mathrm{sp}} \\ r_{\mathrm{ps}} & r_{\mathrm{pp}} \end{bmatrix} \begin{bmatrix} a_{\mathrm{s}} \\ a_{\mathrm{p}} \end{bmatrix}, \qquad \begin{bmatrix} t_{\mathrm{s}} \\ t_{\mathrm{p}} \end{bmatrix} = \begin{bmatrix} t_{\mathrm{ss}} & t_{\mathrm{sp}} \\ t_{\mathrm{ps}} & t_{\mathrm{pp}} \end{bmatrix} \begin{bmatrix} a_{\mathrm{s}} \\ a_{\mathrm{p}} \end{bmatrix}. \tag{2.5}$$

Co-polarized coefficients have both subscripts identical, but cross-polarized coefficients do not. The square of the magnitude of a reflection or transmission coefficient is the corresponding reflectance or transmittance; thus, $R_{\mathrm{sp}} = |r_{\mathrm{sp}}|^2$ is the reflectance corresponding to the reflection coefficient r_{sp}, and so on. The principle of conservation of energy mandates the constraints $R_{\mathrm{ss}} + R_{\mathrm{ps}} + T_{\mathrm{ss}} + T_{\mathrm{ps}} \leq 1$ and $R_{\mathrm{pp}} + R_{\mathrm{sp}} + T_{\mathrm{pp}} + T_{\mathrm{sp}} \leq 1$, the inequalities turning to equalities only in the absence of dissipation in the region $0 < z < NP$.

2.2 Theory

More generally than is needed for a ChevSTF, let us use

$$\left.\begin{array}{l}\underline{\underline{\varepsilon}}_1 = \underline{\underline{S}}_{\mathrm{y}}(\chi_1) \cdot \left(\varepsilon_{\mathrm{b}_1}\hat{\mathbf{u}}_{\mathrm{x}}\hat{\mathbf{u}}_{\mathrm{x}} + \varepsilon_{\mathrm{c}_1}\hat{\mathbf{u}}_{\mathrm{y}}\hat{\mathbf{u}}_{\mathrm{y}} + \varepsilon_{\mathrm{a}_1}\hat{\mathbf{u}}_{\mathrm{z}}\hat{\mathbf{u}}_{\mathrm{z}}\right) \cdot \underline{\underline{S}}_{\mathrm{y}}^T(\chi_1) \\ \underline{\underline{\varepsilon}}_2 = \underline{\underline{S}}_{\mathrm{y}}(\pi - \chi_2) \cdot \left(\varepsilon_{\mathrm{b}_2}\hat{\mathbf{u}}_{\mathrm{x}}\hat{\mathbf{u}}_{\mathrm{x}} + \varepsilon_{\mathrm{c}_2}\hat{\mathbf{u}}_{\mathrm{y}}\hat{\mathbf{u}}_{\mathrm{y}} + \varepsilon_{\mathrm{a}_2}\hat{\mathbf{u}}_{\mathrm{z}}\hat{\mathbf{u}}_{\mathrm{z}}\right) \cdot \underline{\underline{S}}_{\mathrm{y}}^T(\pi - \chi_2)\end{array}\right\} \tag{2.6}$$

for a periodic multilayer whose unit cell comprises two different CTFs. Furthermore, let L_1 and $L_2 = P - L_1$ be the two layer thicknesses.

After defining the phasors

$$\left.\begin{array}{l}\mathbf{e}(z) = \mathbf{E}(x,y,z)\exp\left[-ik_0\left(x\cos\psi + y\sin\psi\right)\sin\theta_{\mathrm{inc}}\right] \\ \mathbf{h}(z) = \mathbf{H}(x,y,z)\exp\left[-ik_0\left(x\cos\psi + y\sin\psi\right)\sin\theta_{\mathrm{inc}}\right]\end{array}\right\}, \tag{2.7}$$

we find that wave propagation in the two CTFs is governed by the 4×4-matrix ordinary differential equations [25]

$$\left.\begin{array}{l}\frac{d}{dz}\left[\mathbf{f}(z)\right] = i\left[\mathbf{P}(\chi_1; \varepsilon_{\mathrm{a}_1}, \varepsilon_{\mathrm{b}_1}, \varepsilon_{\mathrm{c}_1})\right]\left[\mathbf{f}(z)\right] \\ \frac{d}{dz}\left[\mathbf{f}(z)\right] = i\left[\mathbf{P}(\pi - \chi_2; \varepsilon_{\mathrm{a}_2}, \varepsilon_{\mathrm{b}_2}, \varepsilon_{\mathrm{c}_2})\right]\left[\mathbf{f}(z)\right]\end{array}\right\}, \tag{2.8}$$

where the column 4-vector

$$\left[\mathbf{f}(z)\right] = \left[\hat{\mathbf{u}}_{\mathrm{x}} \cdot \mathbf{e}(z) \quad \hat{\mathbf{u}}_{\mathrm{y}} \cdot \mathbf{e}(z) \quad \hat{\mathbf{u}}_{\mathrm{x}} \cdot \mathbf{h}(z) \quad \hat{\mathbf{u}}_{\mathrm{y}} \cdot \mathbf{h}(z)\right]^T \tag{2.9}$$

and the 4×4 matrix

$$\begin{aligned}\left[\mathbf{P}(\xi; \varepsilon_{\mathrm{a}}, \varepsilon_{\mathrm{b}}, \varepsilon_{\mathrm{c}})\right] = \omega &\begin{bmatrix} 0 & 0 & 0 & \mu_0 \\ 0 & 0 & -\mu_0 & 0 \\ 0 & -\varepsilon_0\varepsilon_{\mathrm{c}} & 0 & 0 \\ \varepsilon_0\frac{\varepsilon_{\mathrm{a}}\varepsilon_{\mathrm{b}}}{\varepsilon_{\mathrm{a}}\cos^2\xi + \varepsilon_{\mathrm{b}}\sin^2\xi} & 0 & 0 & \end{bmatrix} \\ &+ k_0\frac{(\varepsilon_{\mathrm{a}} - \varepsilon_{\mathrm{b}})\sin\theta_{\mathrm{inc}}}{\varepsilon_{\mathrm{a}}\cos^2\xi + \varepsilon_{\mathrm{b}}\sin^2\xi}\sin\xi\cos\xi\begin{bmatrix} \cos\psi & 0 & 0 & 0 \\ \sin\psi & 0 & 0 & 0 \\ 0 & 0 & 0 & 0 \\ 0 & 0 & -\sin\psi & \cos\psi \end{bmatrix} \\ &+ \omega\mu_0\frac{\sin^2\theta_{\mathrm{inc}}}{\varepsilon_{\mathrm{a}}\cos^2\xi + \varepsilon_{\mathrm{b}}\sin^2\xi}\begin{bmatrix} 0 & 0 & \cos\psi\sin\psi & -\cos^2\psi \\ 0 & 0 & \sin^2\psi & -\cos\psi\sin\psi \\ 0 & 0 & 0 & 0 \\ 0 & 0 & 0 & 0 \end{bmatrix} \\ &+ \omega\varepsilon_0\sin^2\theta_{\mathrm{inc}}\begin{bmatrix} 0 & 0 & 0 & 0 \\ 0 & 0 & 0 & 0 \\ -\cos\psi\sin\psi & \cos^2\psi & 0 & 0 \\ -\sin^2\psi & \cos\psi\sin\psi & 0 & 0 \end{bmatrix}.\end{aligned} \tag{2.10}$$

Accordingly,

$$\left[\mathbf{f}(NP)\right] = \left[\mathbf{M}\right]\left[\mathbf{f}(0)\right], \tag{2.11}$$

where the 4×4 matrix

$$[\mathbf{M}] = \Big(\exp\left\{ i \left[\mathbf{P}(\pi - \chi_2; \varepsilon_{\mathrm{a}_2}, \varepsilon_{\mathrm{b}_2}, \varepsilon_{\mathrm{c}_2}) \right] L_2 \right\} \, \exp\left\{ i \left[\mathbf{P}(\chi_1; \varepsilon_{\mathrm{a}_1}, \varepsilon_{\mathrm{b}_1}, \varepsilon_{\mathrm{c}_1}) \right] L_1 \right\} \Big)^N . \tag{2.12}$$

Continuity requirements on the tangential components of the electric and magnetic fields across the interfaces $z = 0$ and $z = NP$ give rise to [25]

$$\begin{bmatrix} t_{\mathrm{s}} \\ t_{\mathrm{p}} \\ 0 \\ 0 \end{bmatrix} = [\mathbf{K}]^{-1} [\mathbf{M}] [\mathbf{K}] \begin{bmatrix} a_{\mathrm{s}} \\ a_{\mathrm{p}} \\ r_{\mathrm{s}} \\ r_{\mathrm{p}} \end{bmatrix} , \tag{2.13}$$

where the 4×4 matrix

$$[\mathbf{K}] = \begin{bmatrix} -\sin\psi & -\cos\psi\cos\theta_{\mathrm{inc}} & -\sin\psi & \cos\psi\cos\theta_{\mathrm{inc}} \\ \cos\psi & -\sin\psi\cos\theta_{\mathrm{inc}} & \cos\psi & \sin\psi\cos\theta_{\mathrm{inc}} \\ -\eta_0^{-1}\cos\psi\cos\theta_{\mathrm{inc}} & \eta_0^{-1}\sin\psi & \eta_0^{-1}\cos\psi\cos\theta_{\mathrm{inc}} & \eta_0^{-1}\sin\psi \\ -\eta_0^{-1}\sin\psi\cos\theta_{\mathrm{inc}} & -\eta_0^{-1}\cos\psi & \eta_0^{-1}\sin\psi\cos\theta_{\mathrm{inc}} & -\eta_0^{-1}\cos\psi \end{bmatrix} . \tag{2.14}$$

The solution of Eq. (2.13) provides the four reflection coefficients and the four transmission coefficients defined in Eqs. (2.5).

When $\psi = 0^\circ$ and $0^\circ \leq \theta_{\mathrm{inc}} \lesssim 30^\circ$, the center wavelength $\lambda^{Br}_{0_{sm}}$ of the Bragg regime of order m is predicted to be [9, 28]

$$\lambda^{Br}_{0_{sm}} = \frac{2}{m} \left(L_1 \sqrt{\varepsilon_{\mathrm{c}_1}} + L_2 \sqrt{\varepsilon_{\mathrm{c}_2}} \right) \cos\theta_{\mathrm{inc}}, \qquad m \in \{1, 2, 3, ...\} , \tag{2.15}$$

for s-polarized incidence. Likewise, the center wavelength $\lambda^{Br}_{0_{pm}}$ of the Bragg regime of order m is predicted to be [9, 28]

$$\lambda^{Br}_{0_{pm}} = \frac{2}{m} \left(L_1 \sqrt{\varepsilon_{\mathrm{d}_1}} + L_2 \sqrt{\varepsilon_{\mathrm{d}_2}} \right) \cos\theta_{\mathrm{inc}} \qquad m \in \{1, 2, 3, ...\} , \tag{2.16}$$

for p-polarized incidence, where

$$\varepsilon_{\mathrm{d}_n} = \varepsilon_{\mathrm{a}_n} \varepsilon_{\mathrm{b}_n} \left(\varepsilon_{\mathrm{a}_n} \cos^2\chi_n + \varepsilon_{\mathrm{b}_n} \sin^2\chi_n \right)^{-1} , \qquad n \in \{1, 2\} . \tag{2.17}$$

Equations (2.15) and (2.16) are predicated on the assumption that the constitutive scalars ε_{a_n}, etc., are frequency independent; otherwise, both equations transform from explicit to implicit equations for the determination of the center wavelengths. One can increase or decrease the pitch by changing L_1 or L_2 accordingly, thereby increasing or decreasing the center wavelength of the Bragg phenomenon.

2.3 Experimental Methods

2.3.1 Fabrication of periodic multilayers comprising CTFs

Each periodic multilayer was fabricated using thermal evaporation [29] implemented inside a low-pressure chamber from Torr International (New Windsor, NY, USA). It contains a quartz crystal monitor (QCM) calibrated to measure the growing thin-film's thickness, a receptacle to hold the material to be evaporated, electrodes to resistively heat the receptacle, and a substrate holder positioned about 15 cm above the receptacle. As the chamber was customized to grow sculptured thin films [25], it contains two stepper motors to control the rotation of the substrate holder about two mutually orthogonal axes.

99.995% pure ZnSe (Alfa Aesar, Ward Hill, MA, USA) was the material of choice due to its high bulk index of refraction and low absorption in the visible spectral regime [30, 31], as well as the ease of evaporation. The manufacturer supplied ZnSe lumps that were crushed into a fine powder. A respirator was worn to avoid the toxic effects of ZnSe on the respiratory system [32]. Approximately 4.2 g of ZnSe powder was packed into a tungsten boat (S22-.005W, R. D. Mathis, Long Beach, CA, USA) that served as the receptacle.

A pre-cleaned glass substrate (48300-0025, VWR, Radnor, PA, USA) was further cleaned in an ethanol bath using an ultrasonicator for 10 min on each side. After removal from the bath, the substrate was immediately dried with pressurized nitrogen gas. A straight line was marked on the substrate to serve as the x axis. The substrate was secured to the substrate holder using Kapton™ tape (S-14532, Uline, Pleasant Prairie, WI, USA), and a shutter was interposed between the receptacle and the substrate holder. By the side of the glass substrate, a silicon wafer was positioned in order to grow a sample for imaging on a scanning electron microscope.

The chamber was pumped down to 1 μTorr. The current was then slowly increased to ~ 100 A, and the shutter was rotated to allow a collimated position of the ZnSe vapor to reach the substrate. The deposition rate as read through the QCM was manually maintained equal to 0.4 ± 0.02 nm s^{-1}. After the deposition was complete, the shutter was rotated to prevent further deposition, the current was brought back to 0 A, the chamber was allowed to cool down for 60 min, and was then exposed to the atmosphere.

Each periodic multilayer was chosen to contain $N = 10$ unit cells. This required fabrication to be done in two stages, with 5 unit cells deposited in each stage. By keeping the substrate stationary for 387 s for the deposition of each CTF, the value of P was targeted to be 310 nm. The substrate was rotated by 180° about a central normal axis passing through it in 0.406 s between the depositions of any two consecutive CTFs. The collimated vapor was directed at an angle $\chi_{v_1} \in (0^\circ, 90^\circ]$ with respect to the plane of the substrate to deposit the first CTF in each period, the corresponding angle being $\chi_{v_2} \in (0^\circ, 90^\circ]$ for the second CTF in each period.

Two samples were fabricated:

- Sample A: $\chi_{v_1} = 20^\circ$ and $\chi_{v_2} = 70^\circ$ were chosen such that Eqs. (2.6) would hold in a way that would allow the exhibition of the Bragg phenomenon. In consequence of $\chi_{v_1} \neq \chi_{v_2}$, the expectation was that $L_1 \neq L_2$ [9]. More general than a ChevSTF, Sample A should be a Bragg mirror.

- Sample B: $\chi_{v_1} = \chi_{v_2} = 20^\circ$ were chosen. The equality of χ_{v_1} and χ_{v_2} would ensure that Eqs. (1.4) and (1.7) hold, and, ideally, $L_1 = L_2$ is expected. Thus, Sample B should be a ChevSTF.

Our choices of χ_{v_1} and χ_{v_2} for Samples A and B were guided by the measured relative permittivity dyadics of CTFs of three different materials [9, 33]. The QCM tooling factors were 184 for Samples A and 273 for Sample B. The tooling factor for Sample A is the tooling factor for a film that has a weighted average of $\chi_{v_1} = 20^\circ$ and $\chi_{v_1} = 70^\circ$. Otherwise the tooling factor and current would have needed adjustment mid-deposition, which would have been difficult to manage.

2.3.2 Optical Characterization

Transmittance and reflectance measurements for both Samples A and B were made no more than 24 h after fabrication. Each sample was kept in a desiccator up until the time of characterization in order to prevent degradation due to moisture adsorption.

The experimental setups for reflection and transmission measurements are described in detail elsewhere [34]. Briefly, light from a halogen source (HL-2000, Ocean Optics, Dunedin, FL, USA) was passed through a fiber-optic cable and then through a linear polarizer (GT10, ThorLabs, Newton, NJ, USA); it was either reflected from or transmitted through the sample to be characterized; and was then passed through a second linear polarizer (GT10, ThorLabs) and a fiber-optic cable to a CCD spectrometer (HRS-BD1-025, Mightex Systems, Pleasanton, CA, USA). The transmittances $T_{\rm ss}$, $T_{\rm ps}$, $T_{\rm pp}$, and $T_{\rm sp}$ were measured for $\theta_{\rm inc} \in [0^\circ,\ 70^\circ]$ and $\psi \in \{0^\circ, 90^\circ\}$, and the reflectances $R_{\rm ss}$, $R_{\rm ps}$, $R_{\rm pp}$, and $R_{\rm sp}$ for $\theta_{\rm inc} \in [10^\circ,\ 70^\circ]$ and $\psi \in \{0^\circ, 90^\circ\}$.

All data were taken in a dark room to avoid noise from external sources. First, the detector measured the intensity $I_{\rm dark}$ when the incident light was switched off, no sample was present, and both polarizers had been removed. Then the intensity $I_{\rm s}$ or $I_{\rm p}$ was measured by the detector with no sample present, the first polarizer set to make the incident light either s or p polarized, and the second polarizer set to pass light of the same linear polarization state. Then, the sample was inserted, the second polarizer was set to make the detected light either s or p polarized, and the intensity $\tilde{I}_{\rm s}$ or $\tilde{I}_{\rm p}$ was recorded. In this way, the measured value of $T_{\rm sp}$ was

$$T_{\rm sp} = \frac{\tilde{I}_{\rm s} - I_{\rm dark}}{I_{\rm p} - I_{\rm dark}}, \tag{2.18}$$

and similarly for the other seven reflectances and transmittances. These measurements were made for $\lambda_0 \in [500, 900]$ nm.

2.3.3 Morphological Characterization

The cross-sectional morphologies of both Samples A and B were characterized using an FEI Nova™ NanoSEM 630 (FEI, Hillsboro, OR, USA) field-emission scanning electron microscope. To get a clear image of morphology away from any edge-growth effects, each sample was cleaved using the freeze-fracture technique. This technique is delicate enough to preserve biological samples [35]. All samples were sputtered with iridium using a Quorum Emitech© K575X (Quorum Technologies, Ashford, Kent, United Kingdom) sputter coater before imaging.

Chapter 3

Results

3.1 Morphology

Figure 3.1 presents a cross-sectional scanning-electron micrograph of Sample A fabricated by setting $\chi_{v_1} = 20°$ and $\chi_{v_2} = 70°$. Eight of the 10 unit cells are clearly evident with $P \simeq 313$ nm. Whereas the nanocolumns in one of the two CTFs in a unit cell are inclined at $36.1°$ with respect to the $+x$ axis, those in the other CTF are inclined at $102.6°$ with respect to the $+x$ axis. Thus, the conditions set forth as Eqs. (2.6) are fulfilled with $\chi_1 \simeq 36.1°$ and $\chi_2 \simeq 77.4°$. Furthermore, $L_1 \simeq 0.25P$ whereas $L_2 \simeq 0.75P$, because χ_{v_1} differs from χ_{v_2}. Sample A is clearly not a ChevSTF. Parenthetically, the inequalities $\chi_1 > \chi_{v_1}$ and $\chi_2 > \chi_{v_2}$ are in consonance with a plethora of morphological data on CTFs [9, 36].

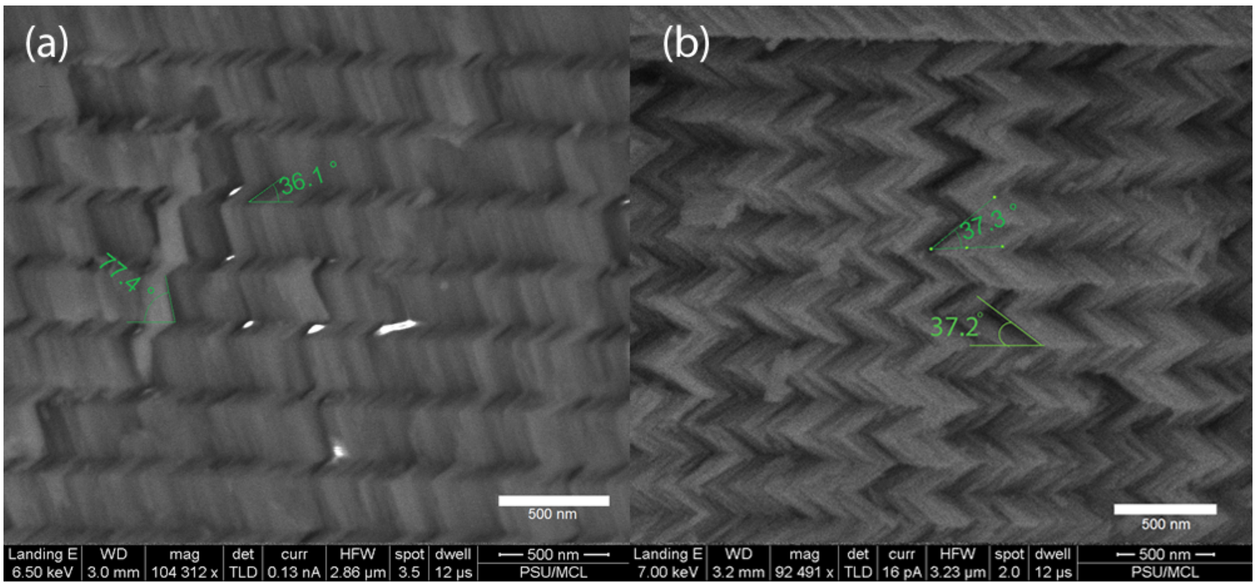

Figure 3.1: Cross-sectional scanning-electron micrograph of Sample A (fabricated with $\chi_{v_1} = 20°$ and $\chi_{v_2} = 70°$) on a silicon wafer on the left and a cross-sectional scanning-electron micrograph of Sample B (fabricated with $\chi_{v_1} = \chi_{v_2} = 20°$) on a silicon wafer on the right.

Figure 3.1 also presents a cross-sectional scanning-electron micrograph of Sample B fabricated by setting $\chi_{v_1} = \chi_{v_2} = 20°$. All 10 unit cells of this sample are clearly evident with $P \simeq 308$ nm and $L_1 \simeq L_2 \simeq P/2$. Whereas the nanocolumns in one of the two CTFs in a unit cell are inclined at $37.3°$ with respect to the $+x$ axis, those in the other CTF are inclined at $142.8°$ with respect to the $+x$ axis. Thus, the conditions set forth as Eqs. (1.4) and (1.7) are fulfilled with $\chi \simeq 37.25°$, and Sample B is a ChevSTF.

3.2 Theoretical Results

Experimental data on the relative permittivity dyadics of CTFs fabricated by evaporating ZnSe are unavailable, but the data on the relative permittivity dyadics of CTFs fabricated by evaporation of TiO_2 are available [33]. The bulk refractive index of ZnSe is 2.5435 at $\lambda_0 = 700$ nm [37], whereas that of TiO_2 is 2.5512 at the same wavelength [38]. The closeness of the two bulk refractive indexes allowed us to substitute ZnSe by TiO_2 for theoretical calculations that can be qualitatively compared with the experimental results.

For $\chi_{v_1} = 20°$, data derived from optical-characterization experiments on CTFs of TiO_2 at $\lambda_0 = 633$ nm [33] are as follows: $\chi_1 = 46.367°$, $\varepsilon_{a_1} = 2.5135$ $\varepsilon_{b_1} = 3.9428$, and $\varepsilon_{c_1} = 3.1525$. Likewise, for $\chi_{v_2} = 70°$, data derived from the same optical experiments are as follows: $\chi_2 = 82.802°$, $\varepsilon_{a_2} = 5.5054$, $\varepsilon_{b_2} = 5.8581$, and $\varepsilon_{c_2} = 5.5785$. For a Bragg mirror comprising TiO_2 CTFs with $\chi_{v_1} = 20°$, $\chi_{v_2} = 70°$, $L_1 = 77.5$ nm, and $L_2 = 232.5$ nm (similar to Sample A), Eqs. (2.15) and (2.16) yield $\lambda^{Br}_{0_{s_2}} = 686.74$ nm and $\lambda^{Br}_{0_{p_2}} = 680.87$ nm when $\theta_{\rm inc} = \psi = 0°$. For a ChevSTF comprising TiO_2 CTFs with $\chi_{v_1} = \chi_{v_2} = 20°$ and $L_1 = L_2 = 155$ nm (similar to Sample B), $\lambda^{Br}_{0_{s_2}} = 550.41$ nm and $\lambda^{Br}_{0_{p_2}} = 540.32$ nm when $\theta_{\rm inc} = \psi = 0°$, according to Eqs. (2.15) and (2.16).

3.2.1 Bragg mirror

In order to present the characteristic features of the Bragg phenomenon, let us begin with the spectrums of all eight remittances calculated for the Bragg mirror comprising TiO_2 CTFs $\chi_{v_1} = 20°$, $\chi_{v_2} = 70°$, $L_1 = 77.5$ nm, and $L_2 = 232.5$ nm (corresponding to Sample A). These remittances are presented as functions of $\lambda_0 \in [400, 1000]$ nm and $\theta_{\rm inc} \in [0°, 90°)$ in Fig. 3.2 for $\psi = 0°$ and in Fig. 3.3 for $\psi = 90°$. For all calculations $N = 30$ was chosen in order to ensure that the Bragg phenomenon is manifested well [12, 39].

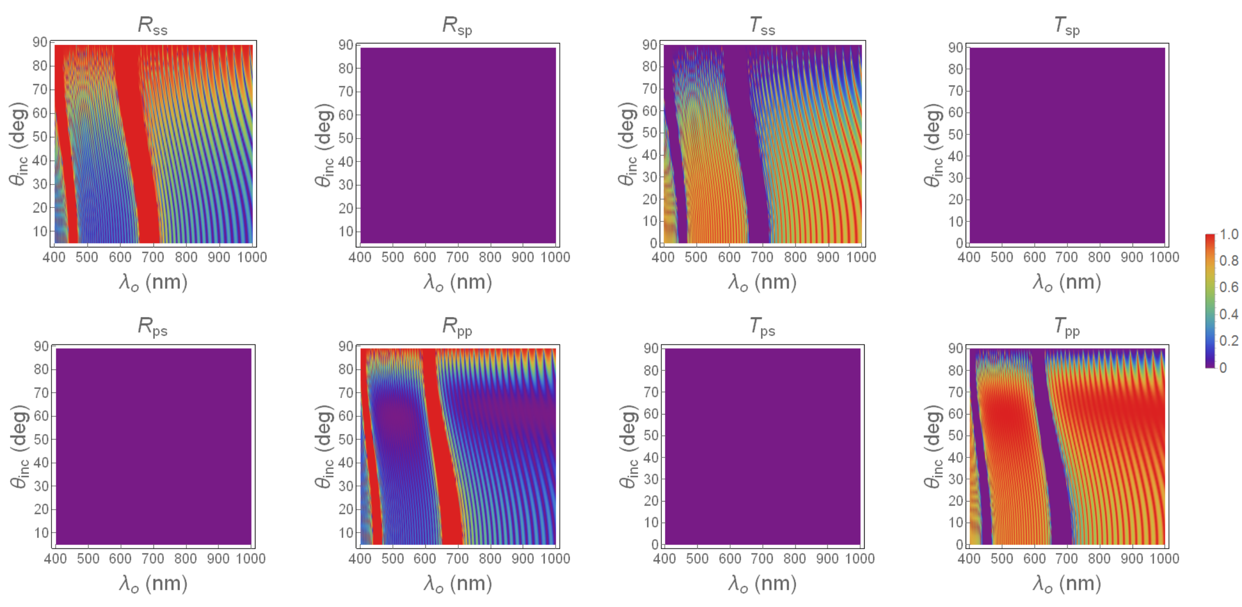

Figure 3.2: Density plots of all four reflectances and all four transmittances calculated as functions of λ_0 and $\theta_{\rm inc}$ for a Bragg mirror comprising TiO_2 CTFs with $\chi_{v_1} = 20°$, $\chi_{v_2} = 70°$, $L_1 = 77.5$ nm, and $L_2 = 232.5$ nm (similar to Sample A), when $\psi = 0°$. All calculations were made with $N = 30$.

Evidence of the Bragg phenomenon of order $m \in \{2, 3\}$ is easy to find in Fig. 3.2. This becomes clear on comparison with the predictions $\lambda^{Br}_{0_{s_2}} = 686.74$ nm, $\lambda^{Br}_{0_{p_2}} = 680.87$ nm, $\lambda^{Br}_{0_{s_3}} = 457.83$ nm, and $\lambda^{Br}_{0_{p_3}} = 453.91$ nm, of Eqs. (2.15) and (2.16) for $\theta_{\rm inc} = \psi = 0°$. The high-reflectance band of order $m \in \{2, 3\}$ in the plot of $R_{\rm ss}$ is slightly redshifted from the high-reflectance band of order $m \in \{2, 3\}$ in the plot of R_{pp}. Furthermore, the Bragg regime of order $m \in \{2, 3\}$ is blueshifted with increase in θ_{inc}. Both high-reflectance bands are mirrored by low-transmittance bands in the plots of T_{ss} and T_{pp}.

With $\lambda^{Br}_{0_{s_1}} = 1373.48$ nm and $\lambda^{Br}_{0_{p_1}} = 1361.74$ nm predicted by Eqs. (2.15) and (2.16), evidence of the Bragg phenomenon of order $m = 1$ is absent from Fig. 3.2. This is not surprising because the plots in this figure were drawn for only $\lambda_0 \in [400, 1000]$ nm. By direct computation, the existence of high-reflectance bands was verified in the plots of R_{ss} and R_{pp}, as well as of low-transmittance bands in the plots of T_{ss} and T_{pp}, that signify the existence of the Bragg phenomenon for $m = 1$.

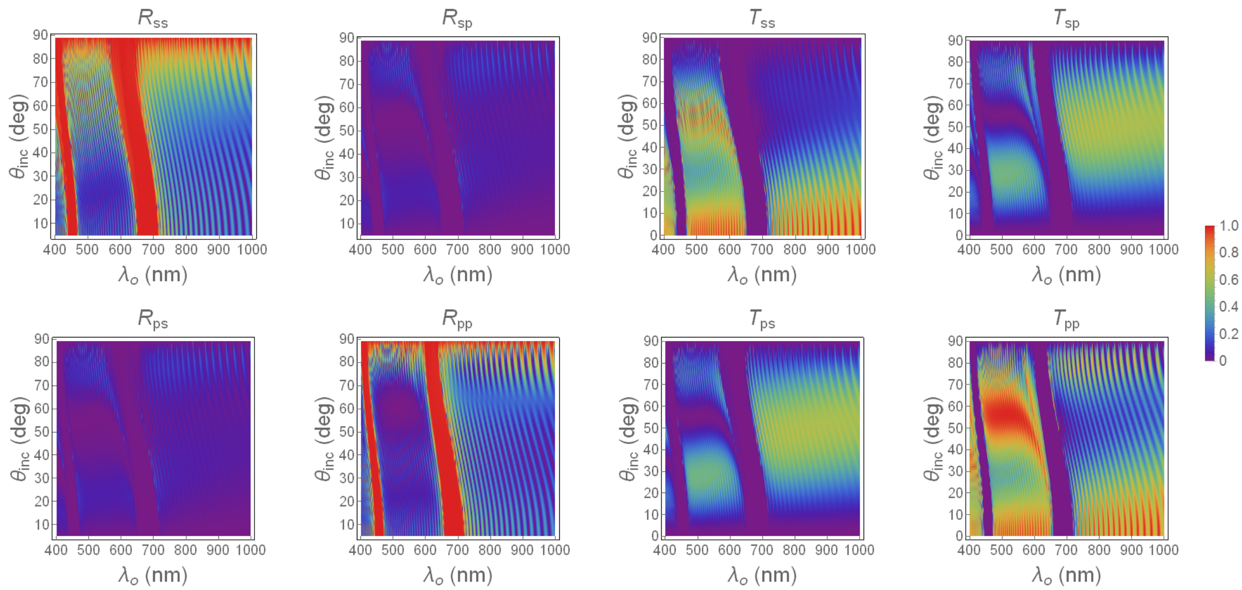

Figure 3.3: Same as Fig. 3.2, except that $\psi = 90°$.

Although no convenient formula is available to predict the center wavelengths for $\psi \in (0°, 180°)$, comparison of Figs. 3.2 and 3.3 suffices to convince that the latter also provides evidence of the Bragg phenomenon of order $m \in \{2, 3\}$. The spectral characteristics of the high-reflectance bands in the plots of R_{ss} and R_{pp} in Fig. 3.3 are the same as in Fig. 3.2. Similar characteristics were found for several values of $\psi \notin \{0°, 90°\}$ (data not presented here).

3.2.2 Chevronic STF

Next, let us present the spectrums of all eight remittances calculated for a ChevSTF comprising TiO_2 CTFs with $\chi_{v_1} = \chi_{v_2} = 20°$ and $L_1 = L_2 = 155$ nm (similar to Sample B). Figure 3.4 presents these remittances as functions of $\lambda_0 \in [400, 1000]$ nm and $\theta_{\mathrm{inc}} \in [0°, 90°)$ when $\psi = 0°$. Although $\lambda^{Br}_{0_{s_2}} = 550.41$ nm and $\lambda^{Br}_{0_{p_2}} = 540.32$ nm when $\theta_{\mathrm{inc}} = \psi = 0°$, according to Eqs. (2.15) and (2.16), no evidence of the Bragg phenomenon of order $m = 2$ exists in Fig. 3.4. Furthermore, although $\lambda^{Br}_{0_{s_1}} = 1100.82$ nm, $\lambda^{Br}_{0_{p_1}} = 1080.64$ nm, $\lambda^{Br}_{0_{s_3}} = 366.94$ nm, and $\lambda^{Br}_{0_{p_3}} = 360.21$ nm are predicted by Eqs. (2.15) and (2.16) for $\theta_{\mathrm{inc}} = \psi = 0°$, it has been verified by direct calculation that the Bragg phenomenon of order $m \in \{1, 3\}$ is also not manifested for the chosen chevronic STF. This is evident from the plot of R_{pp} in Fig. 3.5 for $\lambda_0 \in [400, 1200]$ nm and $\theta_{\mathrm{inc}} \in [0°, 90°)$.

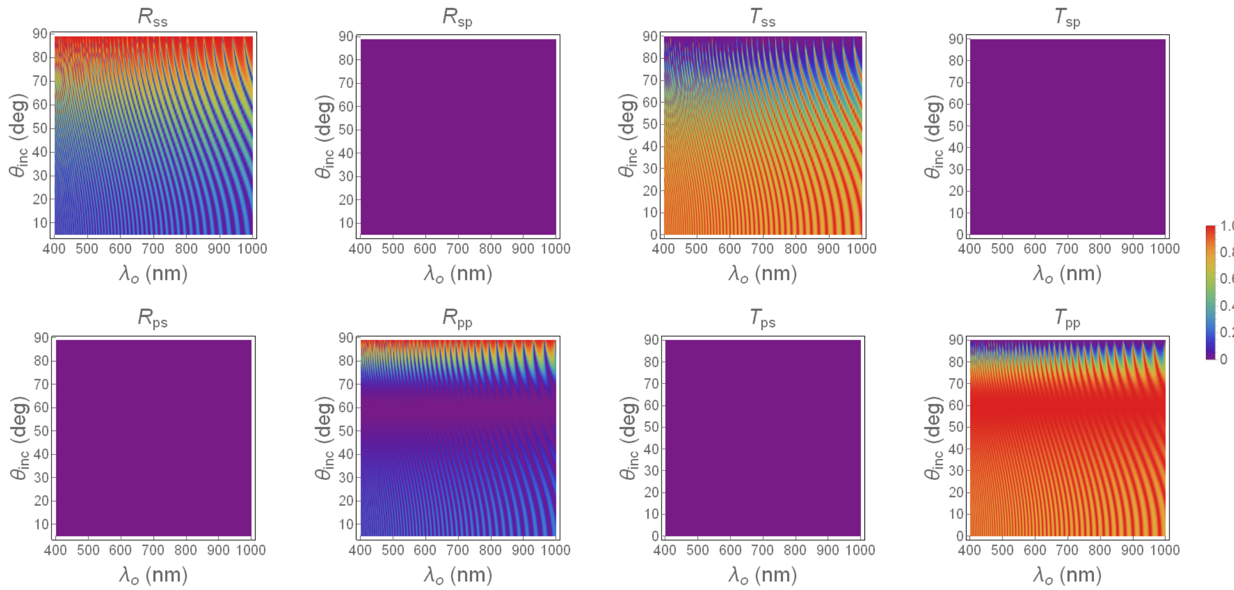

Figure 3.4: Density plots of all four reflectances and all four transmittances calculated as functions of λ_0 and $\theta_{\rm inc}$ for a ChevSTF comprising TiO_2 CTFs with $\chi_{v_1} = \chi_{v_2} = 20^\circ$ and $L_1 = L_2 = 155$ nm (similar to Sample B), when $\psi = 0^\circ$. All calculations were made with $N = 30$.

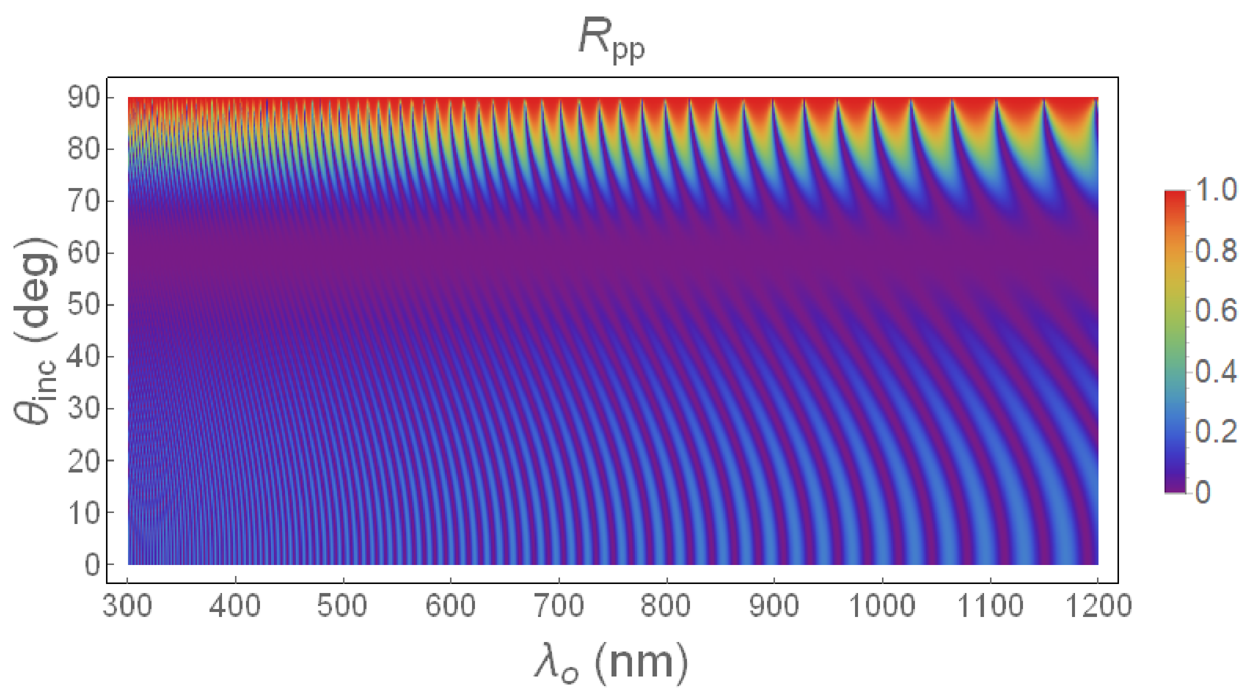

Figure 3.5: Density plot of $R_{\rm pp}$ calculated as a function of λ_0 and $\theta_{\rm inc}$ for a ChevSTF comprising TiO_2 CTFs with $\chi_{v_1} = \chi_{v_2} = 20^\circ$ and $L_1 = L_2 = 155$ nm (similar to Sample B), when $\psi = 0^\circ$.

For $\psi = 90^\circ$, the situation changes somewhat. In Fig. 3.6, the Bragg phenomenon of order $m = 2$ is present in the plots of $R_{\rm ss}$, $R_{\rm pp}$, $T_{\rm ss}$, and $T_{\rm pp}$. But this existence is vestigial at best, as it is evident in very narrow spectral regimes and that too only for $\theta_{\mathrm{inc}} \gtrsim 40°$. The same characteristic holds true for the Bragg phenomenon of order $m \in \{3, 4, 5\}$, as exemplified by Fig. 3.7.

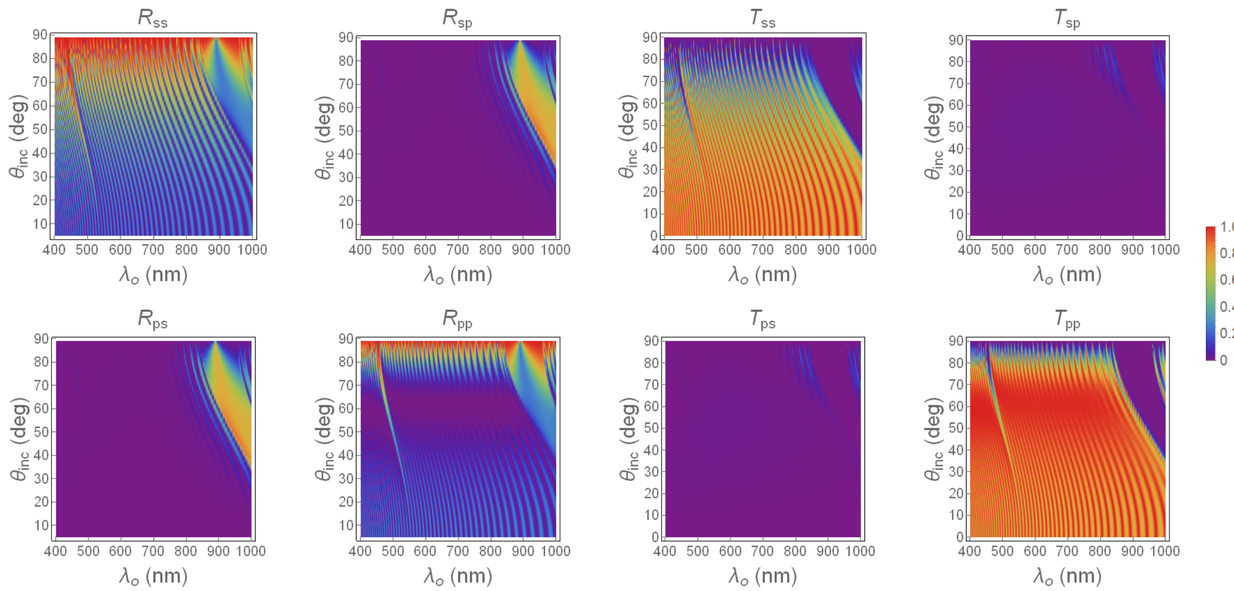

Figure 3.6: Same as Fig. 3.4, except that $\psi = 90°$.

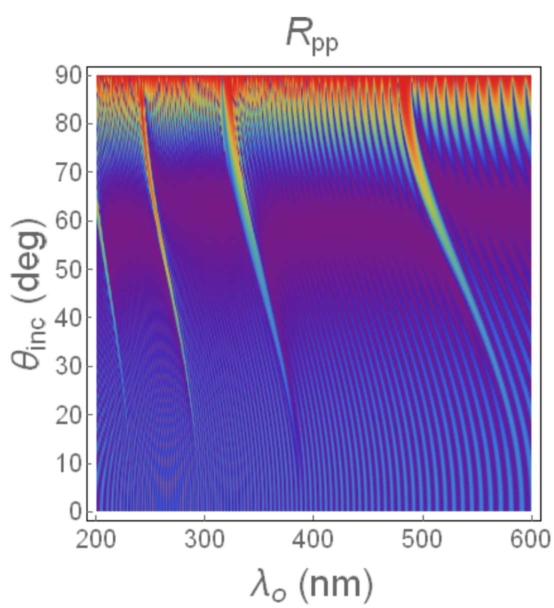

Figure 3.7: Same as Fig. 3.5, except that $\psi = 90°$.

The situation is somewhat different for the Bragg phenomenon of order $m = 1$. High-reflectance bands exist in the plots of R_{ps} and R_{ss} for $\theta_{\mathrm{inc}} \gtrsim 20°$, indicating that reflection is accompanied by a rotation of the vibration ellipse by angles close to $\pm 85°$. In other words, the Bragg phenomenon is accompanied by significant polarization conversion, but even that is not manifested for normal and near-normal incidences.

The foregoing conclusions from examination of computed data can be explained through Eqs. (2.10) and (2.12). For normal incidence, the matrix $[\mathbf{P}(\xi;\varepsilon_\mathrm{a},\varepsilon_\mathrm{b},\varepsilon_\mathrm{c})]$ simplifies to yield

$$\begin{aligned}[\mathbf{P}(\chi;\varepsilon_\mathrm{a},\varepsilon_\mathrm{b},\varepsilon_\mathrm{c})]\Big|_{\theta_\mathrm{inc}=0} &= [\mathbf{P}(\pi-\chi;\varepsilon_\mathrm{a},\varepsilon_\mathrm{b},\varepsilon_\mathrm{c})]\Big|_{\theta_\mathrm{inc}=0} \\ &= \omega\begin{bmatrix} 0 & 0 & 0 & \mu_0 \\ 0 & 0 & -\mu_0 & 0 \\ 0 & -\varepsilon_0\varepsilon_\mathrm{c} & 0 & 0 \\ \varepsilon_0\frac{\varepsilon_\mathrm{a}\varepsilon_\mathrm{b}}{\varepsilon_\mathrm{a}\cos^2\chi+\varepsilon_\mathrm{b}\sin^2\chi} & 0 & 0 & \end{bmatrix}. \qquad (3.1)\end{aligned}$$

Then, both CTFs in the unit cell of a ChevSTF are electromagnetically identical and the structural periodicity of the ChevSTF does not translate into electromagnetic periodicity. Accordingly, the Bragg phenomenon cannot be exhibited for $\theta_\mathrm{inc} = 0^\circ$.

As θ_inc increases, first the second term and then the third and fourth terms on the right side of Eq. (2.10) become increasingly consequential. Therefore, $[\mathbf{P}(\chi;\varepsilon_\mathrm{a},\varepsilon_\mathrm{b},\varepsilon_\mathrm{c})]$ begins to differ from $[\hat{\mathbf{p}}(\pi-\chi;\varepsilon_\mathrm{a},\varepsilon_\mathrm{b},\varepsilon_\mathrm{c})]$, but the difference

$$\begin{aligned}&[\mathbf{P}(\chi;\varepsilon_\mathrm{a},\varepsilon_\mathrm{b},\varepsilon_\mathrm{c})]-[\mathbf{P}(\pi-\chi;\varepsilon_\mathrm{a},\varepsilon_\mathrm{b},\varepsilon_\mathrm{c})] \\ &= 2k_0\frac{(\varepsilon_\mathrm{a}-\varepsilon_\mathrm{b})\sin\theta_\mathrm{inc}}{\varepsilon_\mathrm{a}\cos^2\chi+\varepsilon_\mathrm{b}\sin^2\chi}\sin\chi\cos\chi\begin{bmatrix}\cos\psi & 0 & 0 & 0 \\ \sin\psi & 0 & 0 & 0 \\ 0 & 0 & 0 & 0 \\ 0 & 0 & -\sin\psi & \cos\psi\end{bmatrix} \qquad (3.2)\end{aligned}$$

stems only from the second term on the right side of Eq. (2.10). Hence, the Bragg phenomenon would very weakly exhibited for near-normal incidence. For more appreciable exhibition, θ_inc would have to exceed some threshold value that depends not only on the values of $\varepsilon_{a,b,c}$ and χ but also of ψ. Equation (2.10) also indicates that polarization conversion is not possible when $\sin\psi = 0$ [25].

3.3 Experimental Results

3.3.1 Bragg mirror

Following Sec. 3.2, let us begin with the measured spectrums of all eight remittances of Sample A, which is expected to perform as a Bragg mirror. Figure 3.8 presents the reflectances as functions of $\theta_\mathrm{inc} \in [10^\circ, 70^\circ]$ and transmittances as functions of $\theta_\mathrm{inc} \in [0^\circ, 70^\circ]$ for $\lambda_0 \in [500, 900]$ nm when $\psi = 0^\circ$. As predicted in Sec. 3.2, the Bragg phenomenon of order $m = 2$ is evident as a high-reflectance band each in the plots of R_ss and R_pp and as a low-transmittance band each in the plots of T_ss and T_pp. Let us note R_ss exceeds R_pp in the high-reflectance band, especially as θ_inc increases. The center wavelengths $\lambda_{0_{s_2}}^{Br}$ and $\lambda_{0_{p_2}}^{Br}$ for $\theta_\mathrm{inc} = 0^\circ$ nearly overlap at approximately 700 nm and 695 nm, respectively, in the plots of T_ss and T_pp. The Bragg phenomenon of order $m \neq 2$ lies outside the spectral range of our apparatus.

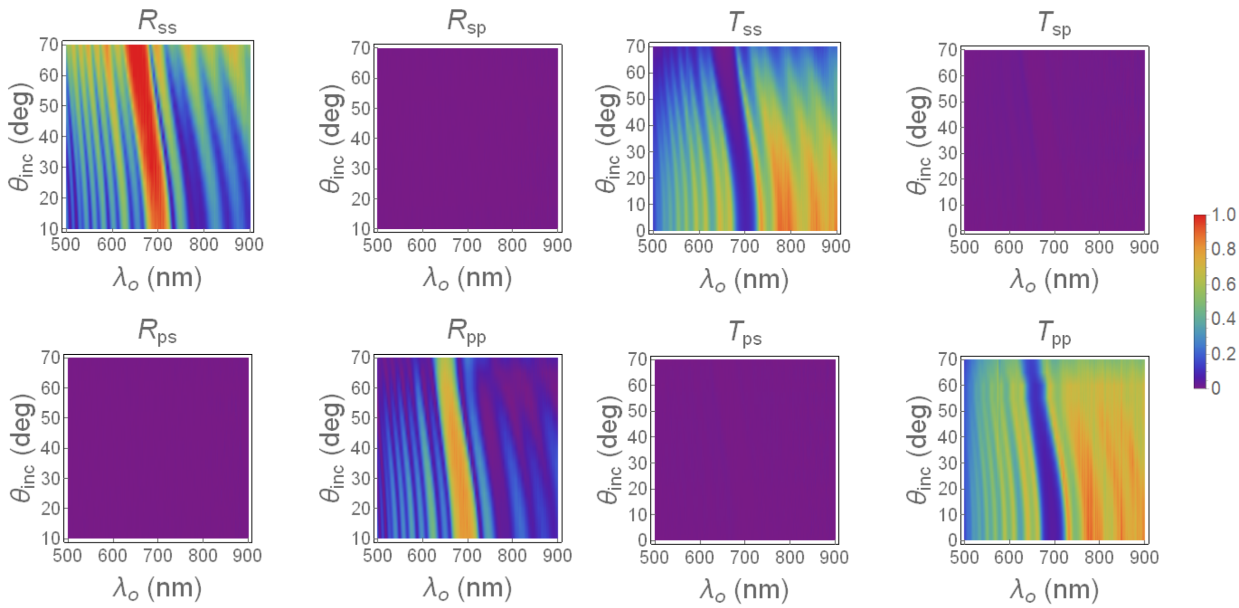

Figure 3.8: Density plots of all four reflectances and all four transmittances measured as functions of λ_0 and θ_{inc} for Sample A (see Fig. 3.1) when $\psi = 0°$.

Figure 3.9 presents the measured remittances of Sample A when $\psi = 90°$. Again, the Bragg phenomenon of order $m = 2$ is evident in the plots of R_{ss}, R_{pp}, T_{ss}, and T_{pp}. The center wavelengths are $\lambda^{Br}_{0_{s_2}} = 710$ nm and $\lambda^{Br}_{0_{p_2}} = 720$ nm for $\theta_{\text{inc}} = 10°$ are somewhat redshifted with respect to those for $\psi = 0°$ in Fig. 3.8, in contrast to the slight blueshifts suggested by the theoretical results presented in Figs. 3.2 and 3.3.

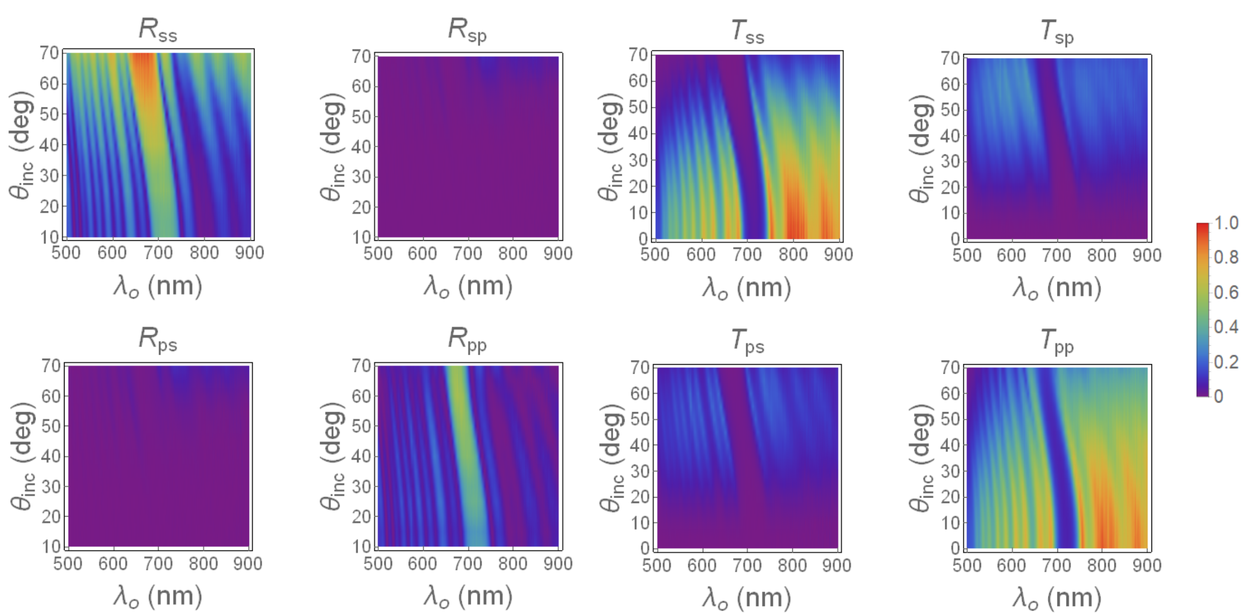

Figure 3.9: Same as Fig. 3.8, except that $\psi = 90°$.

3.3.2 Chevronic STF

Finally, the spectrums of all eight remittances measured for Sample B, which is a ChevSTF, are presented. Figure 3.10 presents these remittances as functions of $\lambda_0 \in [500, 900]$ nm and $\theta_{\rm inc} \leq 70°$ when $\psi = 0°$, and Fig. 3.11 for $\psi = 90°$. Consistently with the theoretical predictions illustrated in Figs. 3.4 and 3.5, no evidence of the Bragg phenomenon exists for $\psi = 0°$ in Fig. 3.8. Even the vestigial Bragg phenomenon of order $m = 2$ predicted in Figs. 3.6 and 3.7 for highly oblique incidence and $\psi = 90°$ is absent in Fig. 3.11. The remittances for $\theta_{\rm inc} > 70°$ could not be measured in order to experimentally investigate the vestigial Bragg phenomenon of order $m = 1$, due to the limitations of our apparatus.

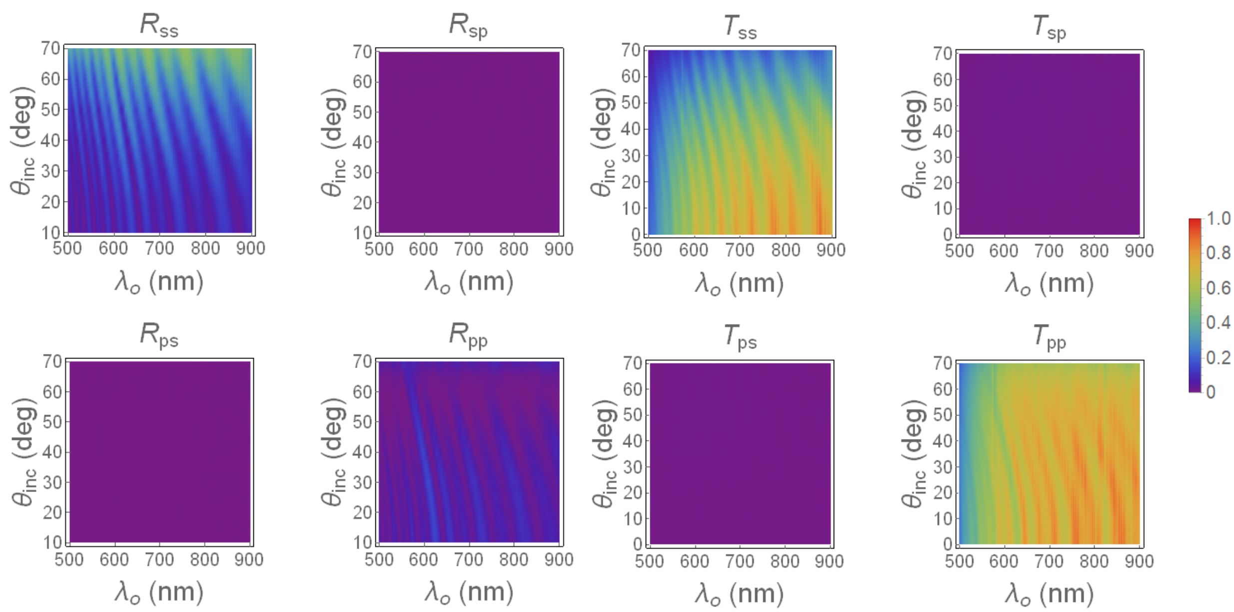

Figure 3.10: Density plots of all four reflectances and all four transmittances measured as functions of λ_0 and $\theta_{\rm inc}$ for Sample B (see Fig. 3.1) when $\psi = 0°$.

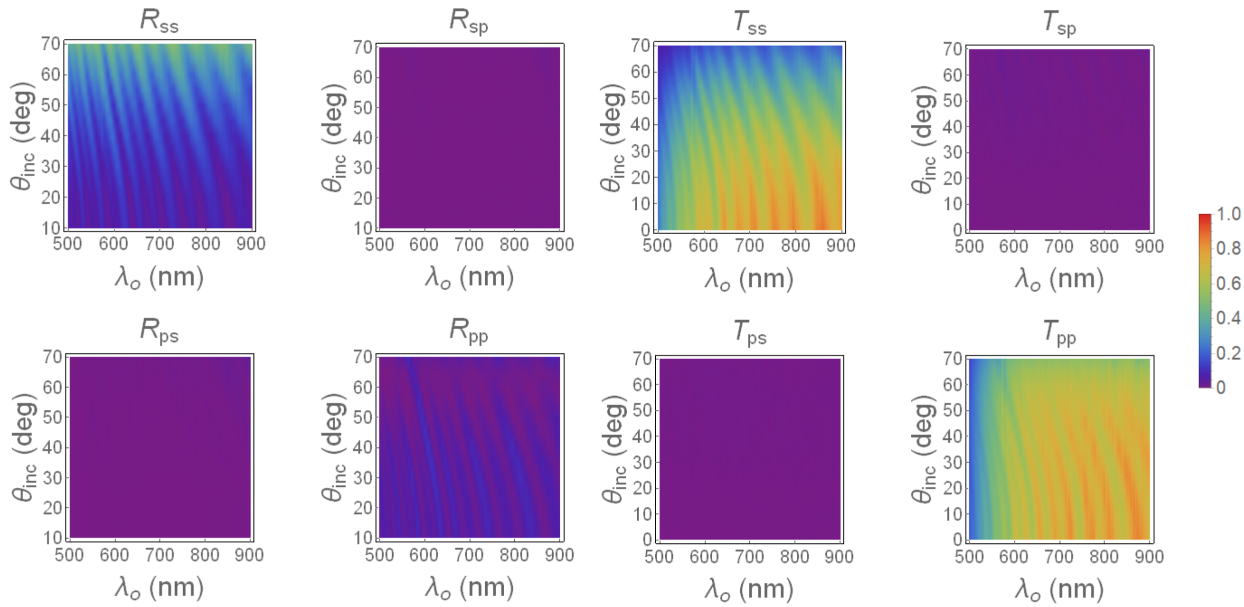

Figure 3.11: Same as Fig. 3.10, except that $\psi = 90°$.

Chapter 4

Conclusion

The unit cell of a chevronic sculptured thin film comprises two identical columnar thin films (CTFs) except that the nanocolumns of the first are oriented at an angle χ and nanocolumns of the second are oriented at an angle $\pi - \chi$ with respect to the interface of the two CTFs. A CTF can be modeled as a homogeneous biaxial dielectric material for optical purposes [9]. Thus, a ChevSTF is a structurally periodic piecewise nonhomogeneous material.

Despite its structural periodicity, it was determined that a ChevSTF does not exhibit the Bragg phenomenon when the wave vector of the incident plane wave lies wholly in the plane formed by the axes of the nanocolumns of the two CTFs (i.e., when $\psi = 0^\circ$). This conclusion was established both theoretically and experimentally, regardless of the polarization state of the incident plane wave.

Theory indicated a vestigial manifestation of the Bragg phenomenon for highly oblique incidence when when the wave vector of the incident plane wave is oriented at an angle $\psi \in (0^\circ, 180^\circ)$ with respect to the plane formed by the axes of the nanocolumns of the two CTFs. Over the limited ranges of the free-space wavelength and the angle of incidence $\theta_{\rm inc}$ of our apparatus, even that vestigial manifestation was not observed. Thus, it has been concluded that the Bragg phenomenon would not be observed if structural periodicity does not lead to appreciable electromagnetic periodicity.

Bibliography

[1] Vikas Vepachedu, Patrick D. McAtee, Akhlesh Lakhtakia, ”Nonexhibition of Bragg phenomenon by chevronic sculptured thin films: experiment and theory,” *Journal of Nanophotonics* **11**(3), 036018 (9 September 2017). http://dx.doi.org/10.1117/1.JNP.11.036018

[2] W. H. Bragg and W. L. Bragg, “The reflexion of X-rays by crystals,” *Proceedings of the Royal Society of London A* **88**(605), 428–438 (1913).

[3] W. H. Bragg, “The intensity of reflexion of X rays by crystals,” *Philosophical Magazine (Series 6)* **27**(161), 881–899 (1914).

[4] P. P. Ewald, “Zur Begründung der Kristalloptik. Teil II: Theorie der Reflexion und Brechung,” *Annalen der Physik* **49**(2), 117–143 (1916).

[5] K. Ohtaka, “Energy band of photons and low-energy photon diffraction,” *Physical Review B* **19**(10), 5057–5067 (1979).

[6] E. Yablonovitch, T. J. Gmitter, and K. M. Leung, “Photonic band structure: the face-centered-cubic case employing nonspherical atoms,” *Physical Review Letters* **67**(17), 2295–2298 (1991).

[7] M. Maldovan and E. L. Thomas, *Periodic Materials and Interference Lithography*, Wiley–VCH, Weinheim, Germany (2009).

[8] Lord Rayleigh, “On the remarkable phenomenon of crystalline reflexion described by Prof. Stokes,” *Philosophical Magazine (Series 5)* **26**(160), 256–265 (1888).

[9] I. J. Hodgkinson and Q. h. Wu, *Birefringent Thin Films and Polarizing Elements*, World Scientific, Singapore (1997).

[10] H. A. Macleod, *Thin-Film Optical Filters, 2nd ed.*, Institute of Physics, Bristol, United Kingdom (2001).

[11] D.M. Mattox, *The Foundations of Vacuum Coating Technology*, Noyes Publications, Norwich, NY, USA, 2003.

[12] P. W. Baumeister, *Optical Coating Technology*, SPIE Press, Bellingham, WA, USA (2004).

[13] [https://en.wikipedia.org/wiki/Dielectric_mirror](accessed February 5, 2018).

[14] [https://en.wikipedia.org/wiki/Thin-film_interference](accessed February 5, 2018).

[15] Laine, Venla E. Photonic Crystals: Fabrication, Band Structure, and Applications. Nova Science Publishers, Hauppauge, N.Y, 2011;2010;.

[16] Trger, F., and SpringerLink (Online service). Springer Handbook of Lasers and Optics. Springer Berlin Heidelberg, Berlin, Heidelberg, 2012;2015;, doi:10.1007/978-3-642-19409-2.

[17] Poladian, Leon. ”Optical Filters.” Wiley Encyclopedia of Telecommunications, edited by John G. Proakis, vol. 3, Wiley, 2003, pp.1722-1733. Gale Virtual Reference Library, http://link.galegroup.com/apps/doc/CX3438600178/GVRL?u=psucic&sid=GVRL&xid=0b29ce18. Accessed 11 Feb. 2018.

[18] Ugale, Sunita P., and V. Mishra. Optimization of Fiber Bragg Grating Length for Maximum Reflectivity, 2011, doi:10.1109/ICCSP.2011.5739375.

[19] H. J. Levinson, Principles of Lithography, Second Edition, SPIE Press, Bellingham, WA (2005).

[20] KNIGHT, JUDSON, and M. C. NAGEL. ”As the ’next-generation’ lithography (NGL) system, is extreme ultraviolet lithography (EUVL) more promising than electron beam projection lithography (EPL).” Science in Dispute, vol. 3, Gale, 2003, pp. 93-100. Gale Virtual Reference Library, http://link.galegroup.com/apps/doc/CX3418700018/GVRL?u=psucic&sid=GVRL&xid=a1c176b6. Accessed 11 Feb. 2018.

[21] [https://www.newport.com/g/dichroic-filters-selection-guide](accessed February 11, 2018).

[22] I. Hodgkinson and Q. H. Wu, “Birefringent thin-film polarizers for use at normal incidence and with planar technologies,” *Applied Physics Letters* **74**(13), 1794–1796 (1999).

[23] H. C. Chen, *Theory of Electromagnetic Waves*, McGraw–Hill, New York, NY, USA (1983).

[24] C. D. Gribble and A. J. Hall, *Optical Mineralogy, Principles and Practice*, University College London Press, London, United Kingdom (1992).

[25] A. Lakhtakia and R. Messier, *Sculptured Thin Films: Nanoengineered Morphology and Optics*, SPIE Press, Bellingham, WA, USA (2005).

[26] G. Y. Slepyan and A. S. Maksimenko, “Motohiro-Taga interface in sculptured thin films—absence of Bragg phenomena,” *Optical Engineering* **37**(10), 2843–2847 (1998).

[27] A. Lakhtakia and R. Messier, “Reflection at the Motohiro-Taga interface of two anisotropic materials with columnar microstructures,” *Optical Engineering* **33**(8), 2529–2534 (1994).

[28] M. Faryad and A. Lakhtakia, “The circular Bragg phenomenon,” *Advances in Optics and Photonics* **6**(2), 225–292 (2014).

[29] S. E. Swiontek and A. Lakhtakia, “Vacuum-metal-deposition and columnar-thin-film techniques implemented in the same apparatus,” *Materials Letters* **142**(1), 291–293 (2015).

[30] [https://www.thorlabs.com/NewGroupPage9.cfm?ObjectGroup_ID=3981] (Februrary 22, 2017).

[31] [http://www.tydexoptics.com/materials1/for_transmission_optics/cvd_znse/] (accessed Februrary 22, 2017).

[32] [https://www.alfa.com/en/catalog/013241/] (accessed Februrary 22, 2017).

[33] I. J. Hodgkinson, Q. h. Wu, and J. Hazel, "Empirical equations for the principal refractive indices and column angle of obliquely deposited films of tantalum oxide, titanium oxide, and zirconium oxide," *Applied Optics* **37**(13), 2653–2659 (1998).

[34] S. Erten, A. Lakhtakia, and G. D. Barber, "Experimental investigation of circular Bragg phenomenon for oblique incidence," *Journal of the Optical Society of America A* **32**(5), 764–770 (2015).

[35] N. J. Severs, "Freeze-fracture electron microscopy," *Nature Protocols* **2**(3), 547–576 (2007).

[36] R. Messier, T. Gehrke, C. Frankel, V. C. Venogopal, W. Otaño, and A. Lakhtakia, "Engineered sculptured nematic thin films," *Journal of Vacuum Science and Technology A* **15**(4), 2148–2152 (1997).

[37] D. T. F. Marple, "Refractive index of ZnSe, ZnTe, and CdTe," *Journal of Applied Physics* **35**(3), 539–542 (1964).

[38] J. R. Devore, "Refractive indices of rutile and sphalerite," *Journal of Optical Society of America* **41**(6), 416–419 (1951).

[39] W. D. St. John, W. J. Fritz, Z. J. Lu, and D.-K. Yang, "Bragg reflection from cholesteric liquid crystals," *Physical Review E* **51**, 1191–1198 (1995).

Academic Vita

EDUCATION

Bachelor of Science, Engineering Science
Minors: Nanotechnology and Physics
Schreyer Honors College
The Pennsylvania State University, University Park, PA
Graduation date: May 2018

JOURNAL PUBLICATIONS

1. **Vikas Vepachedu**, Patrick D. McAtee, Akhlesh Lakhtakia, "Nonexhibition of Bragg phenomenon by chevronic sculptured thin films: experiment and theory," Journal of Nanophotonics 11(3), 036018 (9 September 2017). http://dx.doi.org/10.1117/1.JNP.11.036018

CONFERENCE PROCEEDINGS

1. **Vikas Vepachedu**, Patrick D. McAtee, Akhlesh Lakhtakia, "Non-exhibition of Bragg phenomenon by chevronic sculptured thin films", Proc. SPIE 10356, Nanostructured Thin Films X, 103560W (30 August 2017); doi: 10.1117/12.2272835; http://dx.doi.org/10.1117/12.2272835

HONORS AND AWARDS

Society of Distinguished Alumni Trustee Scholarship	August 2017
Lyle W. and Virginia C. Coffey Scholarship in ESM	July 2017
George S. Wykoff Scholarship	December 2016
John R. and Bernice R. Mentzer Endowed Award	August 2016
James Dipple Trustee Scholarship	August 2015
Dean's List	All semesters

JOB EXPERIENCE

PPG Undergraduate Research Fellowship, PSU — **May 2017 – Aug. 2017**

- Fabricated thin-film based, infrared polarization filters using physical vapor deposition
- Characterized thin films using a scanning electron microscope
- Performed infrared and visible range spectrophotometric characterization of thin films
- Simulated optical properties of said filters in Wolfram Mathematica
- Presented work at research symposium and to PPG engineers

Software Lead, Penn State Lunar Lion Team — **March 2016 – Dec. 2016**

- Led development of Arduino software for automating a prototype lunar lander
- Improved LabVIEW DAQ system for the wireless control of said lander
- Presented details of the software to Penn State officials during a critical design review